# Low Temperature Spectroscopy of Solid State Quantum Systems

by

Erika Janitz

A thesis
presented to the University of Waterloo
in fulfillment of the
thesis requirement for the degree of
Master of Applied Science
in
Electrical and Computer Engineering - Quantum Information

Waterloo, Ontario, Canada, 2013

I hereby declare that I am the sole author of this thesis. This is a true copy of the thesis, including any required final revisions, as accepted by my examiners.

I understand that my thesis may be made electronically available to the public.

**Abstract**

Control and coupling of individual quantum systems remains an important research area in experimental quantum information. Single quantum systems in the solid state offer many attractive properties in terms of isolation and control: strong interaction due to close proximity, and scalability using mature fabrication techniques. Similar to atoms, many solid state quantum systems can couple to photons, offering potential for long-range interaction. Two such candidate systems are the nitrogen vacancy center in diamond, and the nanowire semiconductor quantum dot. These systems can act like isolated atoms in a solid state system, and can serve as sources of indistinguishable photons. This report discusses low temperature excitation of these systems, a regime in which the spectral properties are desirable for applications in quantum information, such as long-distance entanglement.

**Acknowledgements**

Completing my Masters degree was a busy, exciting, and humbling experience. First I would like to thank my family: my mother Clare for her support ( and for taking several phone calls a day when I first moved to Cambridge), and my sister Gretta for her confidence in my abilities. I also want thank my boyfriend Eric for his love and patience over the last year.

I would like to thank my supervisor, Dr. Majedi, for giving me the opportunity to split my time between Waterloo and Harvard. Also, my Waterloo office-mates: Amin Eftekharian for his sage advice, and Milad Khoshnegar who I worked with on the nanowire quantum dot project.

I owe many thanks to Marko Loncar for taking me into his group at Harvard, and introducing me to new projects. I am particularly indebted to Jennifer Choy for having me as an apprentice, and teaching me everything I know about confocal microscopy and fabrication. Finally I would like to thank Srujan Meesala for continuing work on the resonant excitation setup in my absence, and becoming a brother-in-arms during our late night measurements.

Finally, I want to thank all of my friends at IQC and Harvard, who have become incredibly dear to me over the last year.

# Table of Contents

# List of Figures

# Chapter 1

# Introduction

This report discusses low temperature spectroscopy for two different solid state quantum systems: the nitrogen vacancy (NV) center in diamond and the semiconductor nanowire quantum dot. These solid-state quantum systems feature optical transitions that can act as a source of indistinguishable photons, which are important for applications in quantum information processing and cryptography.

The first section discusses the implementation of a resonant excitation spectroscopy setup for NV centers. High efficiency devices for optical control of these defects in diamond have been realized in the form of diamond nanowires and plasmonic cavities. So far, these devices have been operated at room temperature, a regime unsuitable for many applications in quantum information. This project involved creating a low temperature resonant excitation setup for observing NV center spectral properties at high resolution in several high efficiency devices. Such high efficiency sources of indistinguishable photons are required for NV spin entanglement schemes based on two-photon interference.

The second section discusses the design, simulation, fabrication, and testing of an anti-reflection coating for diamond. Several applications for NV centers rely crucially on collection efficiency, or the percentage of photons emitted by the defect that can be collected by an objective lens. Anti-reflection coating is shown to overcome total internal reflection

at the air-diamond interface, increasing the number of photons collected. This technology was coupled with a plasmonic cavity device to improve the modest collection efficiency.

The final section of this report discusses some preliminary spectroscopic measurements for a novel InAsP nanowire quantum dot design. These devices have unprecedented spectral properties due to variety of innovations. A novel fabrication technique ensures excellent structural characteristics, and crystallographic purity. Additionally, the material composition and device design ensure high photon output efficiency and extremely narrow emission linewidth. Some preliminary experimental measurements are presented, and future directions for the project are discussed.

# Chapter 2

# Resonant Excitation Spectroscopy for NV Centers in Diamond Devices

The NV center consists of a substitutional nitrogen atom with an adjacent vacancy in the diamond lattice. It exists in two charge states: the neutral $NV^0$ and the negatively charged $NV^-$. The neutral $NV^0$ has three electrons from dangling carbon bonds and two unpaired electrons from the substitutional nitrogen, resulting in a total spin of $S = 1/2$. The negatively charged $NV^-$ has one additional electron, obtained from a nitrogen atom, or some other donor in the diamond lattice. The even number of electrons results in an integer ground state spin ($S = 1$). Attractive spin and optical properties in the context of quantum information have so-far been observed only for the negatively charged $NV^-$, which is referred to for the remainder of the report and shortened to NV for brevity.

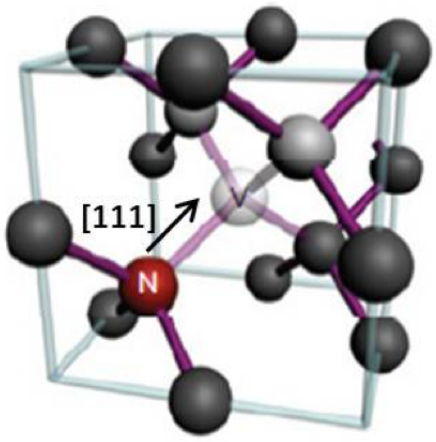


Figure 2.1: An NV center defect in the diamond lattice [1]

The NV center has emerged as a promising qubit candidate in recent years. Due to the wide bandgap of diamond, this defect can act like an isolated atom in a solid state system. With access to mature fabrication techniques for diamond, it is an attractive candidate for implementations of quantum networks and other on-chip devices. The NV center serves as a stable source of single photons at room temperature [2], [3], with optical transitions that are strongly linked to an electronic spin which has coherence times of up to milliseconds at room temperature [4]. This link offers a method for optical spin preparation and readout. Additionally, spin transitions can be driven coherently through the application of microwave fields. We can extend this control over the electronic spin and couple to proximal nuclear spins [5], [6], [7], which have even longer coherence times (seconds) and can act as registers for quantum information [8].

Ideally, one would be able to mediate interactions between distant defects, and recently there was a demonstration of long distance entanglement between two NV centers [9]. The entanglement protocol involved first entangling the electronic spin of the individual defects with an emitted photon [10]. Entanglement was then generated between the two emitters via two-photon interference [11], [12], where two indistinguishable photons impinge simultaneously on a beamsplitter and coalesce into the same ouput port [13]. Implementing

an efficient entanglement protocol using two-photon interference requires a high efficiency photon source, meaning that a high percentage of photons emitted by the NV center can be captured by collection optics. In addition, an interference based entanglement protocol requires a narrow emission linewidth. This chapter will discuss work toward achieving such a photon source from NV centers in diamond devices. An introduction to NV centers is first provided, followed by a description of high efficiency diamond devices. The experimental design is outlined, and the optical setup is explained. Finally, preliminary experimental results are discussed and future project directions are provided.

## 2.1 The NV Center

### 2.1.1 Electronic Structure

The NV center electronic structure is governed by its $C_{3v}$ symmetry, and is illustrated in Figure 2.2 [14]:

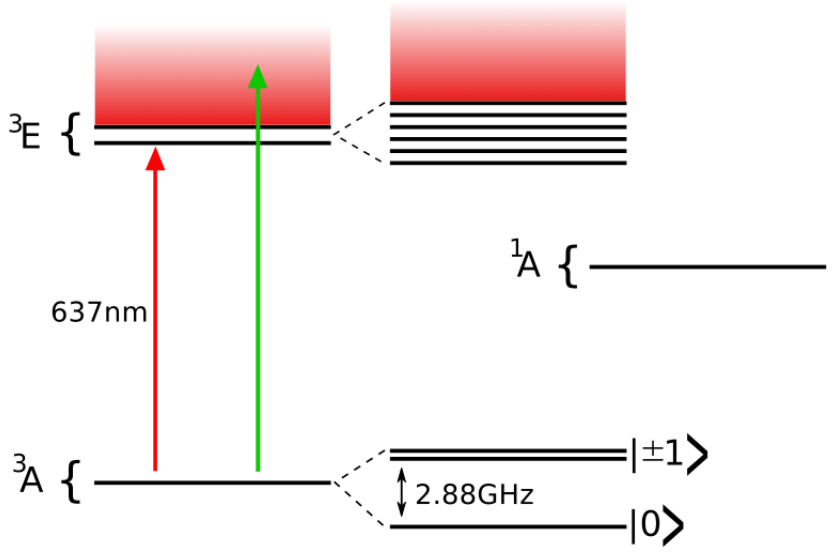


Figure 2.2: The NV center electronic structure. The red arrow indicates the zero phonon line transition between ground and excited states, and the green arrow represents above-band excitation resulting in some phonon scattering.

The NV ground state is a spin triplet ($^3A_2$), with a zero-field splitting of 2.88 GHz into a spin singlet ($m_s = 0$) and doublet ($m_s = \pm 1$) via spin-spin interaction [15]. The excited $^3E$ state is also a spin triplet, with Photoluminescence (PL) emission consisting of a ZPL transition at 637 nm, and a broad red-shifted phonon sideband extending up to 800 nm. The $^3E$ excited state is an orbital doublet, with degeneracy lifted by non-axial strain into two ($E_x, E_y$) orbital branches, where each branch is further composed of the three spin projections [16], [17]. If only spin-conserving transitions are considered, the excited state can exhibit six resonant lines under optical excitation (at low temperature, in low strain samples) [18]. In addition, there is a metastable $^1A_1$ state located between the ground and excited states that has some associated infrared transitions, but is considered dark for the purpose of this report [19]. Intersystem crossing is non-radiative and highly spin-selective, and shelving occurs primarily for $m_s = \pm 1$ spin projections [20]. Decay from the metastable state occurs primarily into the $m_s = 0$ ground state, representing a non-cycling transition through this dark singlet state. This non-cycling transition can be used

for spin preparation into the $m_s = 0$ ground state with high probability [15]. This process also facilitates room-temperature readout of electronic spin state via the spin-dependent photoluminescence (PL) rate. NV centers polarized in either $m_s = \pm 1$ emit less light as they cycle through the dark state more frequently.

### 2.1.2 Optical Excitation

PL spectra from an NV center reveals a narrow zero phonon line (ZPL) transition at 637 nm corresponding to a direct transition from the ground to excited state, and a red-shifted emission referred to as the phonon sideband, seen in Figure 2.3:

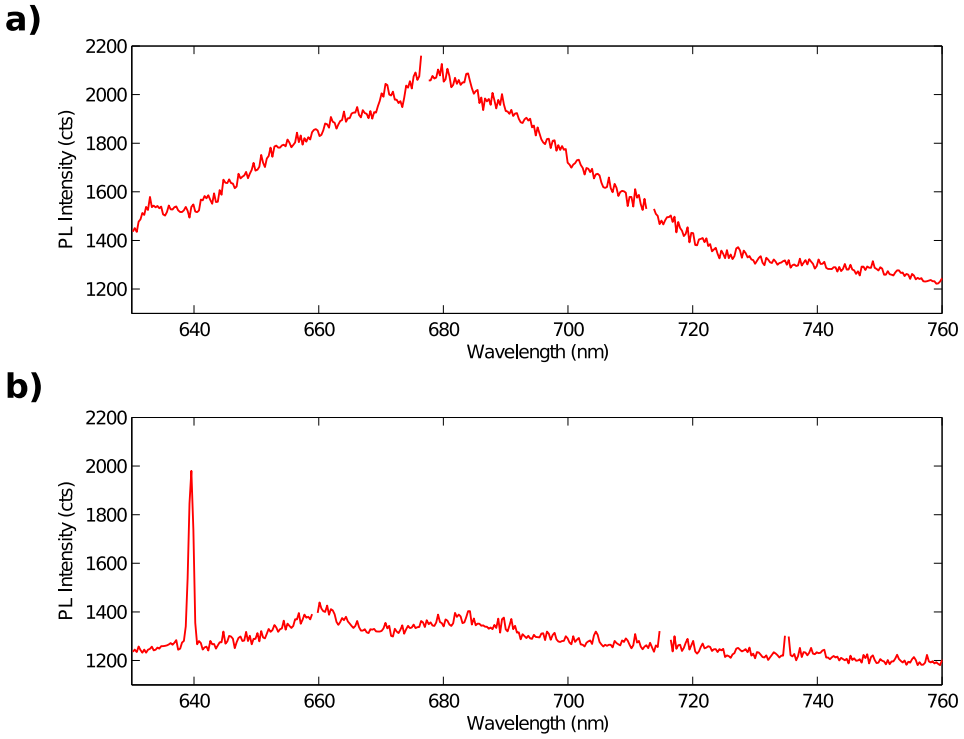


Figure 2.3: Low resolution spectra taken from an NV device in the Loncar Lab at a) room temperature, b) low temperature.

At room temperature (Figure 2.3a) the ZPL transition is broadened and almost completely obscured by the phonon sideband. As the sample is cooled to liquid helium temperature (4 K), many phonon interactions can be frozen out, revealing a narrow ZPL (Figure 2.3b). This transition can be fourier-transform limited (13 MHz) for naturally occurring NV centers in bulk diamond, and can serve as a source of indistinguishable photons. Recently, there has been success in achieving these narrow linewidths for NV center created via implantation by tuning implantation and annealing parameters [1].

The spectra seen in Figure 2.3 were taken using off-resonant optical excitation (532 nm green laser). This illumination is more energetic than the NV center transitions, and phonons are induced in addition to the optical emission. We measure the resulting emission using a spectrometer (Horiba iHr 550), which has at best 0.02 nm resolution. With such coarse resolution, it is impossible to fully resolve the narrow ZPL transition at low temperature, and we are unable to characterize several properties of interest such as the intrinsic linewidth and spectral stability. To resolve these properties it is necessary to implement a resonant excitation scheme, where the NV center is excited with a red laser on resonance with the ZPL transition, and the red-shifted emission from the phonon sideband is collected. One major benefit to this scheme is the nearly zero off-resonant excitation, resulting in resolution that is truly limited by the laser linewidth (∼100kHz).

### 2.1.3 Photoionization

As mentioned in Section 2, the NV center exists in two charge states: the neutral $NV^0$ and negatively charged $NV^-$, where attractive spin and optical properties have so far been observed only in the negatively charged $NV^-$ [21]. The NV center charge state is transient and depends on several factors; to ensure the defect remains in the desired charge state, it is important to understand and control these parameters.

The first parameter to consider is proximity of the defect to the diamond surface. Shallow NV centers are required for many applications in quantum information and magnetometry. Unfortunately, defects close to the surface can suffer from electron depletion due to electron

acceptors at the air-diamond interface, making it hard to maintain the negatively charged state. In fact, the neutral $NV^0$ is the preferred charge state for defects located within 200nm of the surface [22]. Candidates for this electron acceptor layer include graphitic $sp^2$ bonds at the diamond surface [21], and hydrogen termination [23]. Selective oxidation has been shown to increase the density of negatively charged NV centers close to the diamond surface [21], and fluorination was recently proposed as another method of achieving the correct charge state [24]. Oxygen termination can be achieved by boiling diamond in a 1:1:1 solution of nitric, sulphuric, and perchloric acid, and annealing the diamond in an oxygen environment.

Additionally, the NV center charge state can be controlled through the laser excitation sequence. Resonant excitation leads to extremely efficient deionization of the negatively charged NV center into the neutral charge state. The rate of deionization has a nearly quadratic dependence on excitation power, suggesting a two-photon process; a possible mechanism is discussed in Ref. [25]. In addition, the probability of ionization increases with resonant pulse duration. To combat this effect, photoinduced electron transfer can be controlled using off-resonant, high-power laser illumination (532 nm, 1 mW). This process re-ionizes the neutral defect on a time scales from hundreds of nanoseconds to microseconds [26], [27]. Conversely, the defect will relax back to the neutral state in darkness. The reionization process involves an excitation of local charges, freeing electrons to ionize the NV center. The large spread in time constants associated with the ionization process is due to the inhomogenous environment of the diamond lattice [27]. It is therefore important to minimize the resonant laser power over long scans, and alternate resonant pulses with an off-resonant pump laser to ensure the defect remains ionized.

## 2.2 High Efficiency Devices

Remote entanglement schemes relying on two-photon interference require a high output of indistinguishable photons [12]. The number of photons emitted by an NV center can be increased in two ways: first, fabricated nanostructures in diamond can assist in overcoming total internal reflection (TIR) at the diamond surface. More of the emitted photons can

then be captured by collection optics. Secondly, nanostructured cavities can couple to NV centers to modify their radiative lifetime via the Purcell effect, thereby increasing the number of photons emitted by the defect. Top-down fabrication techniques developed by the Loncar group at Harvard University have been used to generate large arrays of devices that show increased output efficiency and enhanced radiative emission for NV centers in diamond.

### 2.2.1 Diamond Nanowires

The first high collection efficiency device created by the Loncar group was the diamond nanowire waveguide, discussed thoroughly in Ref. [28]. These devices are fabricated from commercially available type Ib diamond using electron-beam lithography and reactive ion etching [29]. The result is a large array of nanowires, roughly 200 nm in diameter and 2 $\mu$m tall (Figure 2.4).

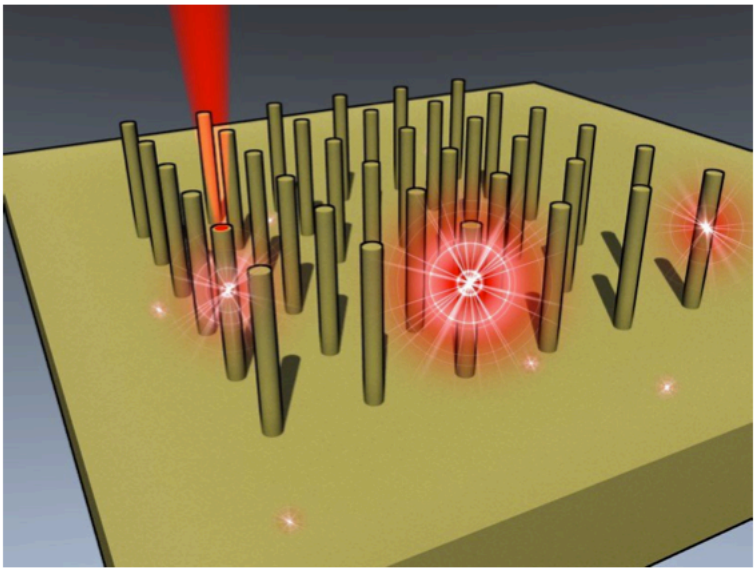

Figure 2.4: An Illustration of NV centers emitting in diamond nanowires [1]

Nanowires containing NV centers are identified as bright spots using a confocal microscope and verified as single photon emitters using a Hanbury Brown and Twiss (HBT) setup.

Coupling the NV center to a diamond nanowire increases the photon emission in two ways: first, the waveguide facilitates efficient optical pumping through more efficient coupling. An order of magnitude less pump power is required to optically saturate a defect. Secondly, the NV center far-field emission pattern is modified, facilitating photon collection into an objective lens. Measured photon counts for NV centers in diamond nanowires exceed $10^5$ counts per second (cps), compared to $10^4$ cps in bulk diamond. Three-dimensional finite-difference time-domain simulations predict that up to 40% of emitted photons can be collected from an NV center emitting in a diamond nanowire, compared to only 3% in bulk diamond, with a comparable radiative lifetime.

### 2.2.2 Plasmonic Apertures

The second device of interest is the diamond-silver plasmonic aperture, discussed in Ref. [30]. These structures are composed of diamond nanoposts (180 nm in height with radii ranging from 50 nm-65 nm) coated with 500 nm of silver, forming a plasmonic cavity. These structures are fabricated using similar top-down techniques as the diamond nanowires. NV centers contained within the cavities are optically accessed through the planar diamond surface on the reverse side of the diamond.

The plasmonic cavity increases the spontaneous emission rate of coupled NV centers via the Purcell effect; a six-fold reduction in radiative lifetime was observed over NV centers in bulk diamond [30]. Photon counts on the order of $10^5$ cps were recorded for these devices, comparable with the rates achieved from the diamond nanowires. However, simulations predict that only 4-5% of emitted photons can captured by collection optics, suggesting the need for further structural optimization to improve collection efficiency.

### 2.2.3 Plasmonic Apertures with Gratings

Collection efficiency for the plasmonic aperture devices can be improved with the addition of gratings, discussed in Ref. [31]. Silica rings were defined around diamond nanoposts via electron-beam lithography to introduce corrugations in the silver capping layer, acting

as a silver grating. These gratings were engineered to coherently scatter surface plasmons, increasing the fraction of optical power in the critical cone of emission from the planar diamond surface. Experiments confirm that the collection efficiency for a silver aperture with an optimized grating structure is improved by roughly two-fold.

## 2.3 Experiment Design

Two experiments were designed to test our high efficiency diamond devices: a single-shot measurement, and a spectral stability characterization measurement.

### 2.3.1 Single-shot Measurement

The first experiment of interest is the single-shot measurement. For this experiment, a short, high-power green laser is first applied ($\sim$10 $\mu$s, $\sim$1 mW) to ensure the NV center is negatively charged and to initialize the electronic spin in the $m_s = 0$ state. The pump laser is followed by a high-power, single-frequency resonant laser pulse ($\sim$1 $\mu$s, $\sim$1 $\mu$W), and photons are collected during this time. This sequence is repeated $N$ times to gather photon statistics. The resonant laser frequency is then increased in steps to cover the frequency range of interest. The single-shot pulse sequence is illustrated in Figure 2.5:

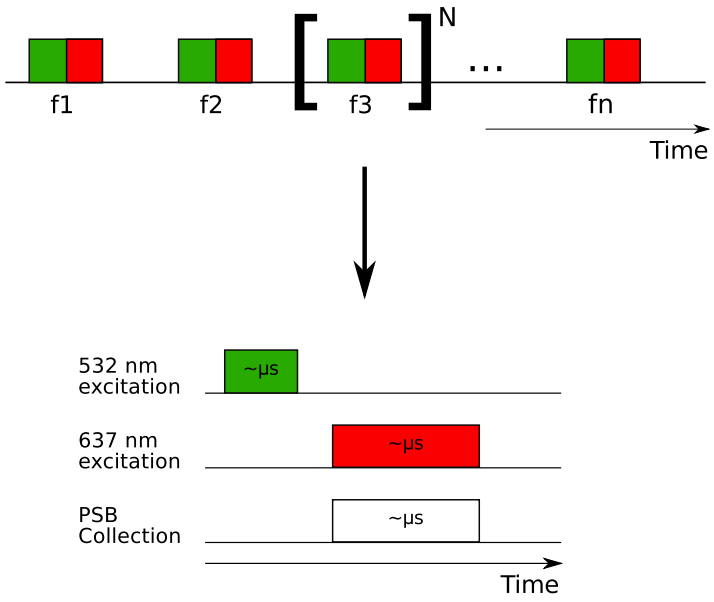


Figure 2.5: Single-shot measurement pulse sequence.

The premise of this experiment is to gather statistics on the average number of photon counts per resonant "shot" at a particular frequency. The red measurement window should be tailored to ensure that at most, one photon is measured. Such a measurement is commonly used for spin-readout [32]. This experiment offers no information about the intrinsic linewidth, as the green pump laser causes spectral diffusion and frequency jumps [33]. The distribution of spectral jumps is related to the local charge density surrounding the NV center, which varies largely from defect to defect [34].

### 2.3.2 Spectral Stability Measurement

The second experiment of interest is a spectral stability characterization. For this experiment, a high-power green laser is first applied ($\sim$10 $\mu$s, $\sim$1 mW) to ensure the NV center is negatively charged and to initialize the electronic spin in the $m_s = 0$ state. The pump laser is followed by a low-power, long resonant laser pulse ($\sim$10 ms, $\sim$10 nW) where the frequency is scanned over the range of interest and photons are collected during this

time. This sequence is repeated $N$ times to gather photon statistics. The spectral stability measurement pulse sequence is depicted in Figure 2.6:

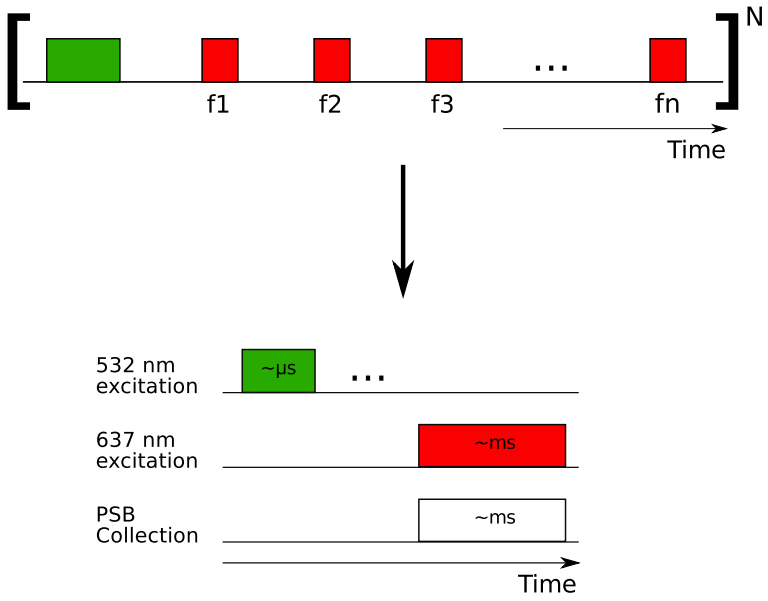


Figure 2.6: Spectral stability characterization pulse sequence.

This measurement can be used to determine the intrinsic ZPL linewidth using data from a single scan. After repumping, large spectral jumps are observed; the magnitude of the spectral jumps vary from center to center due to inhomogenieties in local environment. Resonant excitation converts the $NV^-$ to $NV^0$ with a rate proportional to applied power [34], so extremely low laser power must be used for long scans. To compensate for the low excitation power, a long photon collection time is used.

## 2.4 Experimental Setup

Experiments involving single NV centers rely crucially on the ability to optically address individual defects. For applications in quantum information, this requires a high resolution

microscope, where defects can be resonantly excited at low temperature. This section discusses the necessary optical setup, as well as experimental control and data acquisition.

### 2.4.1 Low Temperature Confocal Microscope

A home-built confocal microscope offers the small focal volume required to optically access individual NV centers. The focal volume is proportional to the laser spot size on the sample, which is $\sim$ 650 nm for the setup discussed in this report. A schematic of the microscope can be seen in Figure 2.7:

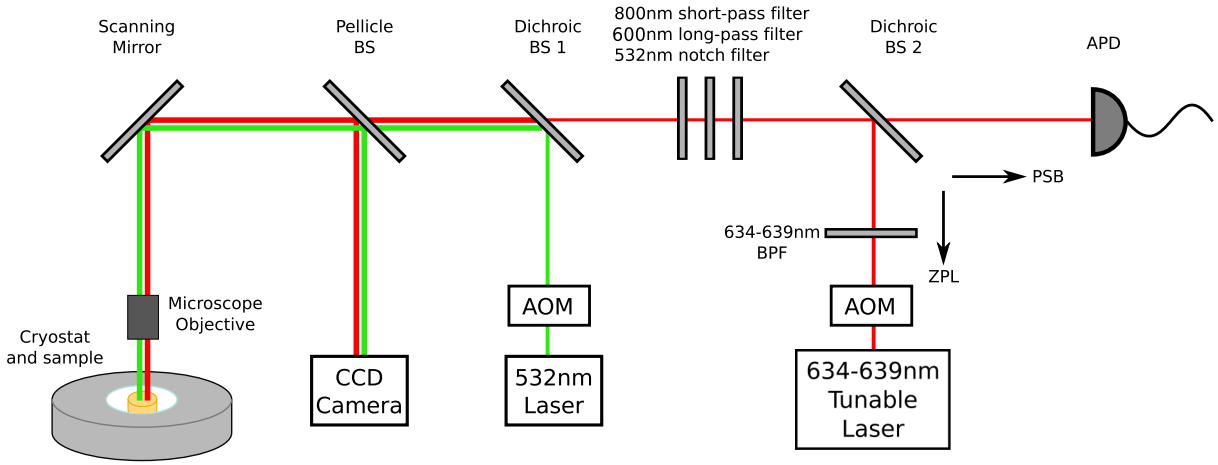


Figure 2.7: The confocal microscope setup.

An existing confocal microscope was augmented to include a customized Janis ST-500 helium flow cryostat, compatible with the 4 mm working distance of our objective lens. Diamond samples are mounted on a copper cryostat coldfinger using silver paste, and the sample chamber is then evacuated to a pressure below $10^{-4}$ Torr. Helium is transferred from a dewer to the cryostat with a transfer line, which cools the coldfinger and sample to 4K. The sample is observed through a low-loss quartz window using a 0.6 NA objective lens. Coarse positioning of the sample is achieved by mounting the cryostat on an x-y linear stage and adjusting the z-axis of the objective lens. Low magnification imaging for

positioning purposes is done with a CCD camera. High resolution imaging is achieved by scanning the laser across a 40X40 $\mu$m section of the sample using the scanning mirror.

The setup contains two excitation arms and one collection arm. Off-resonant green excitation is used to initialize the NV center into the correct charge and spin state. Resonant excitation is performed using a tunable external cavity grating laser (634-639 nm, New Focus Velocity TLB 6304), and band-pass filter is included to suppress residual laser sidebands (Semrock FF01-636/8-25). Both excitation lasers are modulated using a laser switching setup which is discussed in detail in Section 2.4.2, and simplified with acousto-optical modulators (AOMs) in this diagram. The red-shifted phonon sideband emission passes through a series of filters, including a 600 nm long-pass filter and 800 nm short-pass filter to remove background emission, followed by a 532 nm notch filter to remove residual laser light. Two dichroic filters are used to separate the excitation laser light from the NV center emission. The green laser is separated using a 552 nm cut-off dichroic beamsplitter (Semrock LM01-552-25), and the resonant laser is separated using a 654 nm cut-off dichroic beamsplitter (Semrock Di01-CR635-25X36). Photon counts are acquired using a single mode fiber (SMF) coupled to an avalanche photodiode (APD, PerkinElmer Single Photon Counting Module SPCM-AQRH). This can be replaced with a fiber beamsplitter if photon statistics are of interest, or coupled to a spectrometer to obtain spectral data.

### 2.4.2 Laser Modulation Setup

To achieve the laser pulse sequences discussed in Section 2.3, we require a method of modulating the laser output in time; for this we use the laser switching setup shown in Figure 2.8:

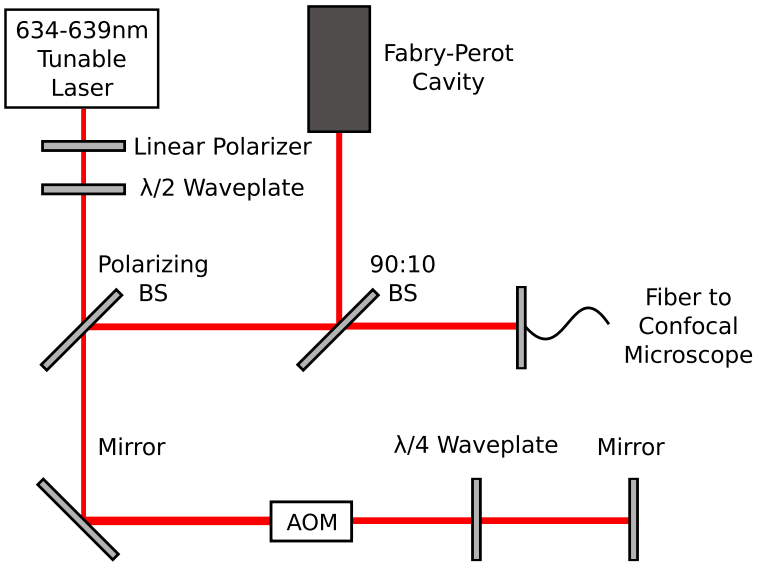


Figure 2.8: The resonant laser modulation setup.

The output of the continuous wave (CW) tunable red laser first passes through a linear polarizer and a $\lambda/2$ waveplate, where all of the polarized light is transmitted. The light is then directed with a mirror into an AOM (Crystal Technology Inc. 3200-144), where it is either transmitted or deflected depending on a programmable input signal. These devices have rise times of tens of nanoseconds and can modulate light on a similar time scale. This modulation allows us to achieve discrete laser pulses in time. The light is guided back through the AOM, making two passes through a $\lambda/4$ waveplate, and it is completely reflected by the polarizing beamsplitter. For the off-resonant green laser, all of this light is then coupled to an optical fiber and sent to the the confocal setup for excitation purposes. For the case of the resonant laser, the reflected light instead passes through a 90:10 beamsplitter, where 90% of the light is coupled to a fiber and sent to the confocal setup. The remaining 10% of the outgoing light is directed into a Fabry-Perot cavity (Thorlabs SA200-5B), which is used to calibrate the frequency range scanned by the tunable laser. The cavity has a known free spectral range of 1.5 GHz and photodiode termination. Every time the laser comes into resonance with the cavity, a current is

generated and read by control software. This allows us to precisely calibrate the NV center ZPL linewidth in terms of the scanning laser input parameters.

### 2.4.3 Experimental Control and Data Acquisition

A block diagram outlining experimental control is given by Figure 2.9:

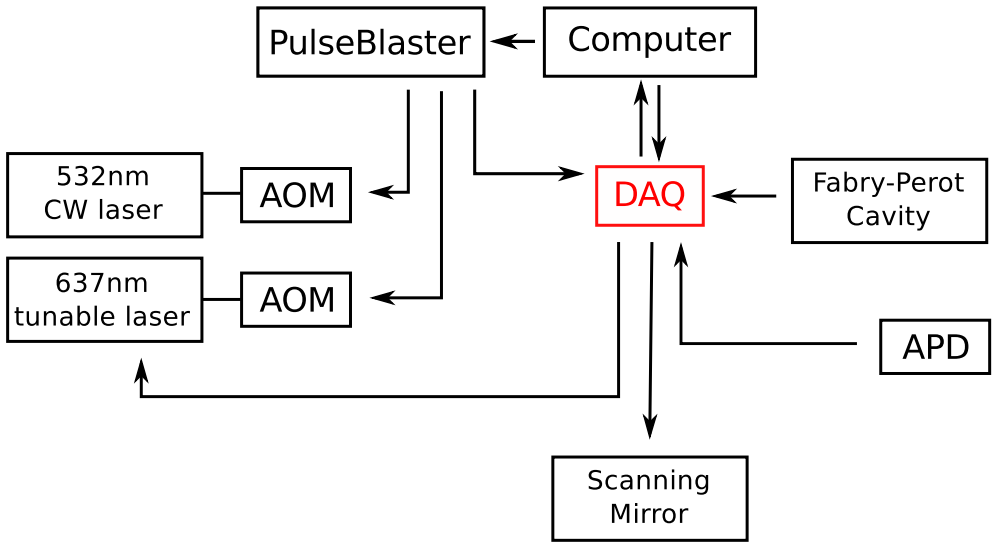


Figure 2.9: Experimental Control Block Diagram.

All experimental control and data acquisition is achieved using a LabView program. A National Instruments data acquisition device (NI DAQ PCI-6229) is used for analog voltage control of the tunable red laser and scanning mirror. In addition, the DAQ receives an analog voltage input signal from the Fabry-Perot cavity, and TTL voltage input from the APD module. Experimental timing is governed using a TTL pulse generator, or "PulseBlaster" (SpinCore Technologies PulseBlasterESR-PRO-500). The PulseBlaster output is used to modulate the AOMs, and to provide timing queues for data acquisition.

## 2.5 Preliminary Experimental Results

Preliminary experimental results were taken using a diamond nanowire sample, with an implantation depth of 100 nm. The sample underwent a tri-acid clean and three-step anneal process (described in Ref. [1]) prior to testing, to ensure oxygen termination at the diamond surface. A preliminary low temperature confocal scan (Figure 2.10) shows bright circles corresponding to the tops of nanowires. The background fluorescence from the sample is incredibly high ($\sim$ 30 kcps), about one third of the emission one would expect from the brightest devices containing NV centers. It was therefore necessary to map out the sample at room temperature, identifying promising devices before mounting the sample in the cryostat.

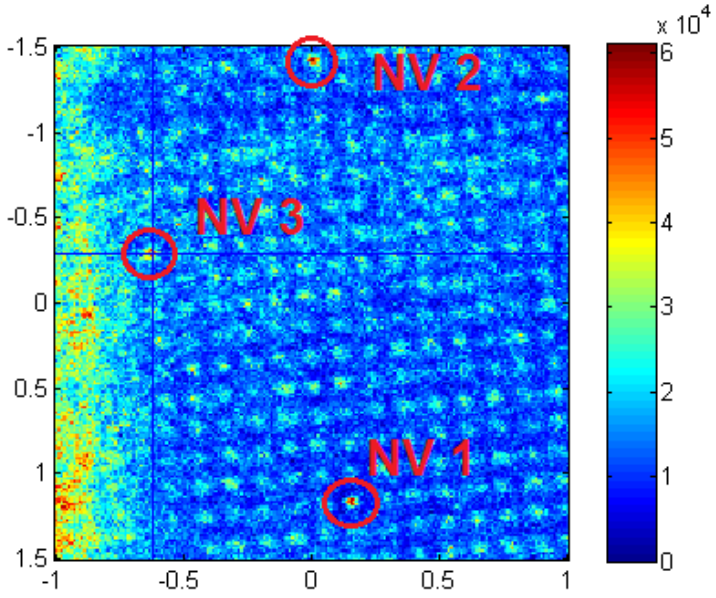


Figure 2.10: A confocal scan of a diamond nanowire sample. Three devices containing NV centers are identified.

### 2.5.1 Power Dependent Spectra

ZPL spectra was measured for a 1 $\mu$m diameter device, with a center wavelength of 637 nm. Excitation power was varied to determine the power required to sufficiently excite the NV center before severe broadening of the ZPL occured. Figure 2.11 is an example of a single-shot measurement where the acquisition time was lengthened to decrease measurement shot noise; this was done for analysis of some unusual spectral features.

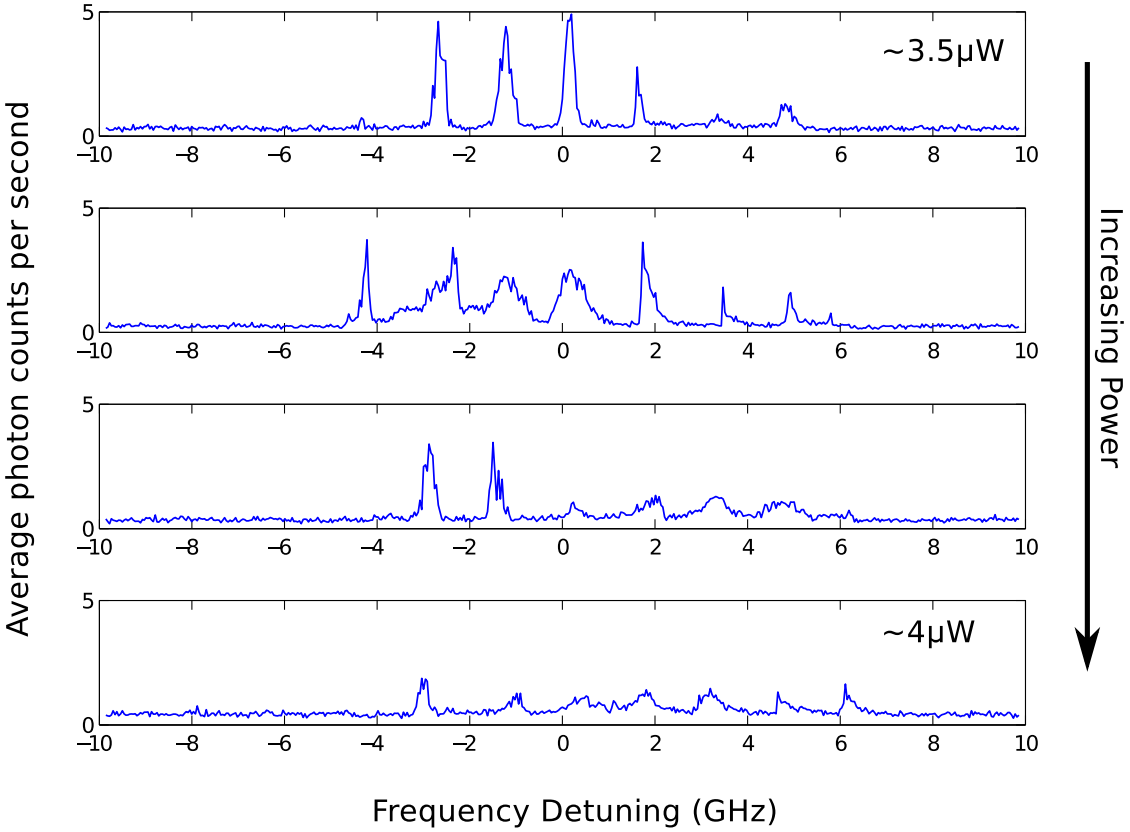


Figure 2.11: Power dependent spectra for a diamond nanowire device.

One would expect to see a single resonance representing the ZPL [35], but instead there are 6-8 resonant modes appearing in these measurements. The peaks span over an $\sim$ 8 GHz range, and seem to have a non-trivial power dependence. The peak spacing does not

appear to be constant, or device dependent, suggesting that these artifacts are not caused by device parameters or due to some cavity formed within the setup. In addition, spectra only appear over a small range of powers ($\sim 2-5\ \mu$W) and are not observed in background measurements. Temperature dependent spectra was taken to try and pinpoint the cause of these peaks.

### 2.5.2 Temperature Dependent Spectra

Temperature dependent spectra can be seen in Figure 2.12:

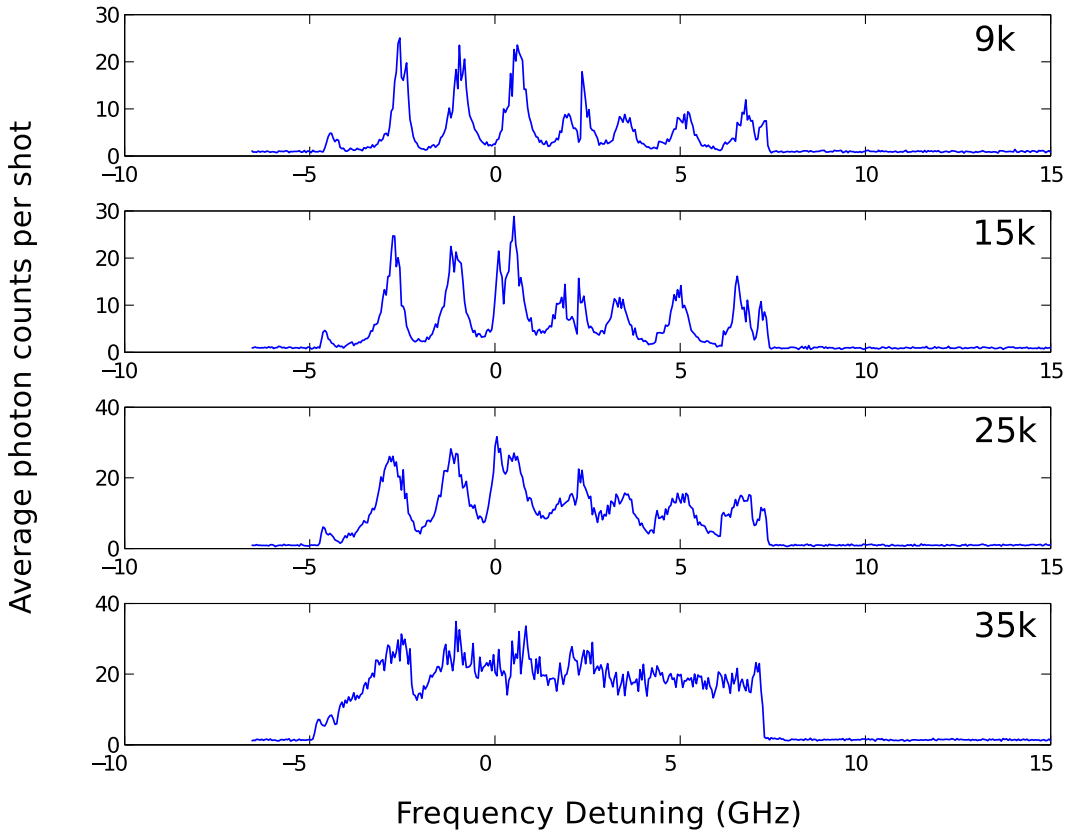


Figure 2.12: Temperature dependent spectra for a diamond nanowire device.

The peak positions appeared to be constant over time for a fixed power. As the temperature was increased from 4 K, broadening of individual peaks began to occur. This temperature dependent broadening indicates that this spectra is indeed ZPL emission [36]. At 40 K the peaks are completely obscured; such severe broadening is expected for the ZPL of naturally occurring NV centers in bulk diamond, and would presumably be worse for implanted samples.

It was determined that the multiple peaks appearing in the ZPL spectra were due to a faulty laser diode in our tunable red laser, causing the laser to have multiple modes that each excite the NV center as the frequency is scanned.

## 2.6 Conclusion and Future Directions

In conclusion, a low temperature resonant excitation setup was created for studying NV center devices at low temperature. A cryostat was integrated into an existing confocal microscope, and an additional red excitation arm was included. Experiment control and data acquistion was achieved through the use of a LabView program, and resonant emission was detected. The next step for this project is to remeasure the power and temperature dependent spectra using the repaired tunable red laser. We expect to see resonant peaks corresponding to the ZPL transition. Additionally, the single-shot measurement and spectral stability characterization should be optimized for our setup.

The next goal involves full characterization of the ZPL transition for a diamond nanowire and plasmonic aperture sample. These devices have never been studied at low temperature, and it is important to understand the effects of fabrication on the NV center spectral properties.

Finally, the creation of a low temperature resonant excitation setup paves the way for many experiments involving NV centers that require indistinguishable photons, such as long-distance entanglement.

# Chapter 3

# Improving Photon Collection Efficiency with Anti-reflection Coating

Several applications for NV centers in diamond rely crucially on collection efficiency, or the percentage of photons emitted by a defect that can be captured by collection optics. The collection efficiency for NV centers in bulk diamond is low, due to the high refractive index contrast between air and diamond ($n_d = 2.4$). Previous approaches for mitigating TIR at the air-diamond interface include the fabrication of solid immersion lenses [37], and nanowire waveguides [28] in the diamond host. Additionally, silver plasmonic apertures fabricated around the NV centers have been shown to decrease the excited state lifetime, resulting in a higher rate of photon emission [30].

In this chapter, the application of an anti-reflection (AR) coating to a plasmonic aperture device is presented as a means of improving the collection efficiency. The coating decreases TIR at the air-diamond interface, allowing more photons to escape the diamond. The theoretical and design considerations are described, followed by a description of the simulation results and fabrication process. The improvement in collection efficiency is demonstrated through a photon intensity saturation measurement and figure of merit calculation.

## 3.1 Theoretical Background

The refraction of photons incident on a diamond-air interface is governed by Snell's Law, where $n_{air} = 1$ and $n_d = 2.4$. The critical angle for TIR can be determined:

$$\theta_c = 24.6^o$$

The critical angle for a photons exiting the diamond substrate is $24.6^o$, and the resulting acceptance cone is very small. We can apply an AR coating to expand the acceptance cone; the simplest implementation is a single-layer film with thickness $\lambda/4n$, where $\lambda$ is the desired wavelength for increased transmission in free-space, and $n$ is the refractive index of the coating. The coating introduces a $\frac{\pi}{2}$ phase shift between light reflected from the coating and the diamond surface, resulting in destructive interference and a decrease in reflection. For the two reflected beams to cancel perfectly they should be of equal intensity, a constraint that is enforced by having the same refractive index ratio at both interfaces [38]:

$$\begin{aligned} \frac{n_{air}}{n_{AR}} &= \frac{n_{AR}}{n_d} \\ \therefore n_{AR} &= \sqrt{n_{air} \times n_d} \end{aligned} \tag{3.1}$$

An ideal coating material for an air-diamond interface would have $n_{AR} = 1.55$.

The simplified structure of a diamond-silver aperture sample with added AR coating is illustrated by Figure 3.1:

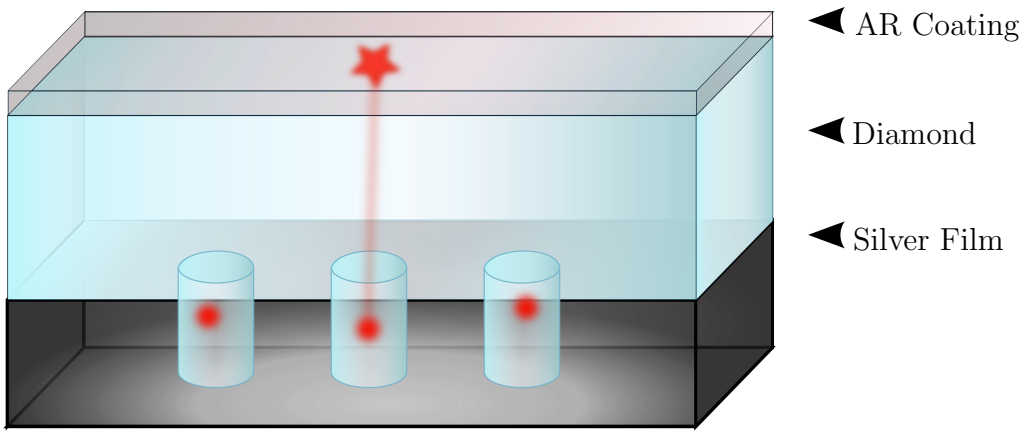


Figure 3.1: The diamond-silver aperture sample with added AR coating.

## 3.2 Design Simulation and Fabrication

One difficulty in fabricating a high-quality AR coating for a particular interface lies in finding a material that satisfies Equation 3.1, and also offers ease of fabrication. $SiO_2$ was chosen for the air-diamond interface as the fabrication procedure is simple and well known. It was previously measured for a similar in-house deposition to have a refractive index of $n = 1.46$, which is reasonably close to our target index of $n = 1.55$. When designing an AR coating, the thickness is determined by the desired wavelength for increased transmissivity according to $t = \lambda/4n$. To maximize the collection efficiency over the broad-band NV center emission, a central wavelength, such as 700 nm, should be chosen.

Different coating thicknesses were evaluated with a transmission/reflection spectra simulation performed by MEEP finite-difference time-domain (FDTD) electromagnetic simulation software [39]. The NV center was modelled as a point source below the diamond-air

interface. The results were averaged over the acceptance cone, and can be seen in Figure 3.2.

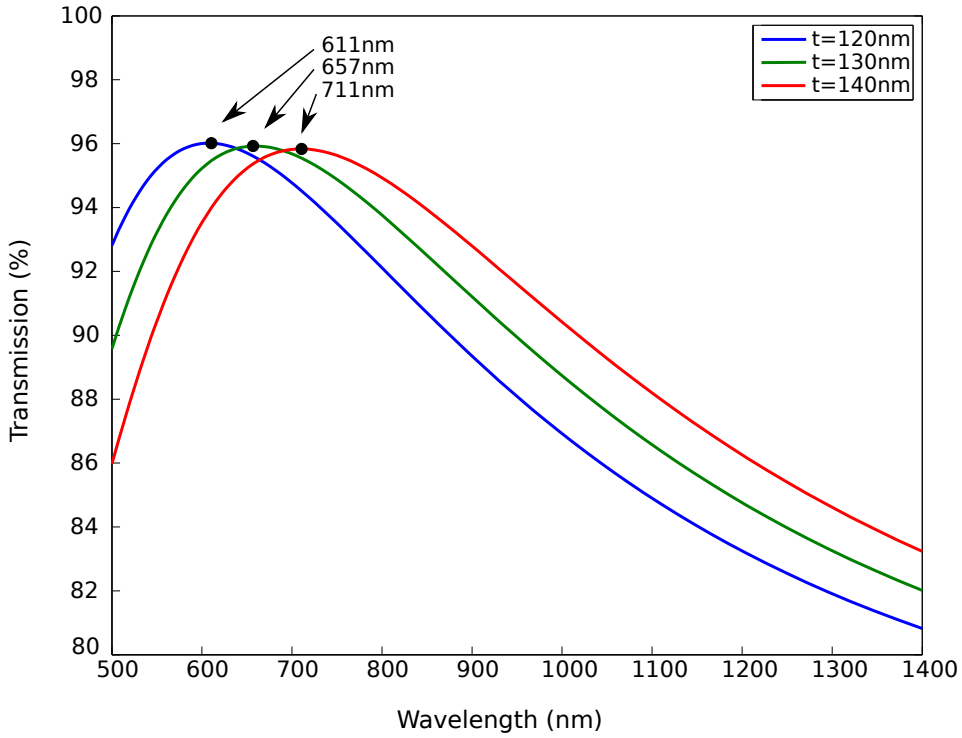


Figure 3.2: Transmission spectra for $SiO_2$ AR coatings of varying thicknesses.

For an AR coating with $t = 120$ nm, one would expect the peak transmission to occur at $\lambda = 4tn = 700$ nm. The simulation results indicate that the peak for $t = 120$ nm actually occurs at 622 nm, a blue-shifted value. This can be explained by comparing the requirements for destructive interference for a beam that is normally incident ($\theta_1 = 0$), to one that is obliquely incident ($\theta_2 > 0$) on the AR coating surface. The phase difference between waves reflected from the first and second surfaces of the coating is described by the following equation [38]:

$$\beta = \frac{2\pi}{\lambda} t \times n_{AR} \times cos\theta_2 \tag{3.2}$$

where $\theta_2$ is the angle of the beam to the normal in the AR coating. The following ratio must be true for a normally incident beam to incur the same relative phase as one that is obliquely incident:

$$\begin{aligned} \frac{\lambda_1}{\lambda_2} &= \frac{cos\theta_1}{cos\theta_2} \\ &= \frac{1}{cos\theta_2} \\ &\geq 1 \end{aligned} \tag{3.3}$$

$$\therefore \ \lambda_1 \geq \lambda_2 \tag{3.4}$$

This inequality implies that for obliquely incident light, the relative phase required for destructive interference occurs for shorter wavelengths than predicted by $\lambda = 4tn$. This relationship results in a blue-shift of the transmission resonance when averaging over the acceptance cone, and consequently a coating thickness of 130 nm was chosen for fabrication.

The $SiO_2$ film was applied with a sputtering process, and the deposition rate was established during an initial run. The coating was then applied to the diamond surface of a plasmonic aperture sample and a larger Si sample used for ellipsometry measurements. The thickness of the film was measured to be 129.55 nm by ellipsometry, with a refractive index of $n_{AR} = 1.47$ at 700 nm. The transmission spectrum for a film with these properties is calculated by FDTD simulation in Figure 3.3.

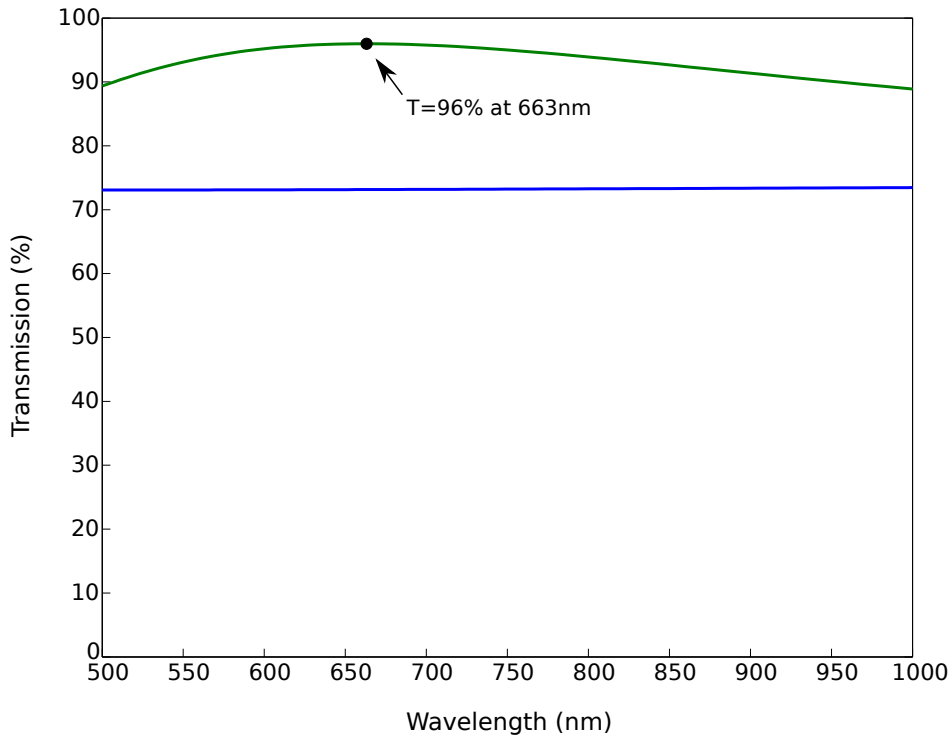


Figure 3.3: Transmission spectra for $SiO_2$ AR coating with $t = 129.55$ nm and $n_{AR} = 1.47$ compared with an uncoated diamond surface.

The AR coating has a peak transmissivity of 96% at 676 nm, which can be compared to ~73% over all visible wavelengths for uncoated diamond.

## 3.3 Saturation of Single Photon Flux

The improvement in collection efficiency offered by the AR coating should be experimentally verified by an increase in photon count rates measured for a device. This improvement can be quantified in terms of two parameters [28]:

- $P_{sat}$ - The optical pump power required to saturate the NV center emission.
- $I_{sat}$ - The maximum number of single photons per second that can be collected from the NV center.

These parameters can be determined experimentally by interpolating the photon count rate at varying laser pump powers. The data should adhere to the following relationship:

$$I(P) = \frac{I_{sat}}{(1 + P_{sat}/P)} \tag{3.5}$$

where $P$ is the optical pump power. At some high pump power ($P_{sat}$), the photon count rate will plateau ($I_{sat}$) due to the finite lifetime of the NV center. With the application of AR coating, we would anticipate a decrease in $P_{sat}$, as a higher percentage of the pump power should penetrate the device interface. Conversely, we would expect an increase in $I_{sat}$, as more of the emitted light from the NV center should be able to escape the diamond surface.

To calculate the improvement in $P_{sat}$ and $I_{sat}$, the photon count rates for an NV center should be recorded at various pump powers before and after the coating is applied. The raw photon counts include some background signal, which varies linearly with pump power. To calculate the background contribution at each pump power, we must extract some data from the photon second order correlation function. The procedure for this calculation is explained in Appendix A. The experimental saturation results are presented in Figure 3.4:

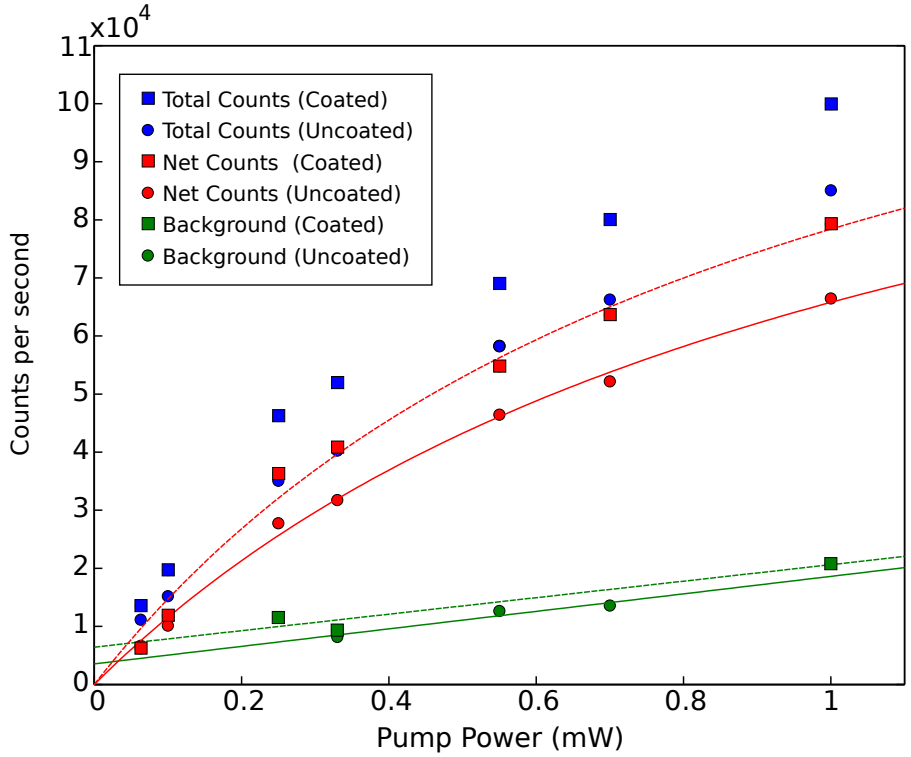


Figure 3.4: Photon saturation curves for the same plasmonic aperture device with (solid red line) and without (dotted red line) AR coating.

Fitting Equation 3.5 to the net photon count data, the following device parameters were calculated:

Uncoated sample: $P_{sat} = 1.1$ mW, $I_{sat} = 138$ kcps

Coated sample: $P_{sat} = 0.93$ mW, $I_{sat} = 151$ kcps

These results represent a roughly 10% and 18% increase in collection and pump efficiencies, respectively. The discrepancy from analytical calculation might be attributed to the fact that our simulation did not take into account the NV center spectrum. In addition, there may be a difference in the thickness of the silica deposited on the diamond surface, and the silicon used for calibration purposes.

## 3.4 Figure of Merit Calculation

Another method of quantifying the improvement in collection efficiency involves comparing the percentage of photons emitted by the NV center that one is able to collect from a coated verses uncoated diamond surface. For this calculation, we model the NV center as a dipole in the [111] diamond crystal plane, beneath the [100] polished surface of the diamond substrate where photons are collected [40] [41]. Because the crystal strain is randomly distributed throughout the sample, one can assume the dipole is randomly oriented in the [111] plane [37]. By averaging over all possible dipole orientations, an average PL intensity distribution for s-polarized and p-polarized emission can be obtained in spherical coordinates [42]:

$$I_s(\theta,\phi) = \frac{1}{16\pi}\Big(\sin^2\theta(2\sin^2\phi + 1)\Big) \tag{3.6}$$

$$I_p(\theta,\phi) = \frac{1}{8\pi}\Big(\cos^2\theta + \frac{1}{\sqrt{2}}\sin(2\theta)\sin\phi + 1\Big) \tag{3.7}$$

We can describe the accessible single photon flux using the following figure of merit [28]:

$$N = \frac{\int^{\lambda}\int_0^{2\pi}\int_0^{\theta_m}\Big[I_s(\theta,\phi)T_s(\theta,\lambda) + I_p(\theta,\phi)T_p(\theta,\lambda)\Big]\Gamma_0(\lambda)\sin\theta d\theta d\phi d\lambda}{\int^{\lambda}\Gamma_0(\lambda)d\lambda} \tag{3.8}$$

- $T_{s,p}$ are the polarization dependent transmission coefficients for the uncoated and coated diamond surfaces calculated by the transfer matrix method.
- $\theta_m = \sin^{-1}(\frac{NA}{n_d})$ is the effective numerical aperture, where $NA$ is the numerical aperture of our objective lens and $n_d$ is the refractive index of diamond [42].
- $sin\theta d\theta d\phi$ is the solid angle defined by the planar diamond surface.
- $\Gamma_0(\lambda)$ is the room-temperature NV fluorescence spectrum, included to emphasize the wavelength dependence of $T_{s,p}$.

For the coated surface, a figure of merit value of $N = 1.77\%$ was obtained, which can be compared to $N = 1.48\%$ for the uncoated surface. The application of the AR coating therefore results in a 19.6% increase in accessible photon flux.

## 3.5 Conclusion

In conclusion, the application of a single-layer AR coating was shown to improve the collection efficiency for an NV center in a silver aperture device. The ideal thickness for a silica coating was first calculated using an FDTD simulation to be 130 nm, and then sputtered onto the planar diamond surface. This increase in efficiency was experimentally verified through a photon saturation measurement, indicating a roughly 10% and 18% increase in collection and pump efficiencies respectively. A figure of merit calculation was then presented to support this result. This increase in collection efficiency is useful for experiments requiring many indistinguishable photons.

# Chapter 4

# Spectroscopy of InAsP Nanowire Quantum Dots

The final section of this thesis discusses a different kind of solid state quantum system: the nanowire quantum dot. Quantum Dots (QDs) are semiconductor nano-devices that are spatially confined in all three dimensions. As the physical size decreases, the energy bands present in bulk semiconductor become discrete energy levels, similar to those of an atom. These devices are optically active, and photon absorption results in generation of electron-hole pairs, or excitons. It is possible to operate in a regime where only one or two excitons are confined within a device, resulting in inherently quantum properties that are of interest for applications in quantum information [43], cryptography [44], and quantum optics [45]. Such applications demand fine control over spectral properties, and over the physical dimensions of the QD structure.

The most-studied type of semiconductor QD is the self-assembled type, where surface strain between the QD and capping material causes random island nucleation, referred to as the Stranski-Krastanow growth mode [46]. The inherently stochastic nature of this growth process has traditionally made it difficult to control the size, shape, density, and position of these structures. This chapter discusses a novel nanowire QD design that allows for a high degree of control over the QD position and dimensions during the growth process

[47]. Excellent structural properties translate to narrow emission linewidths, an important property for all aforementioned applications. First the design and fabrication of these devices is discussed, followed by preliminary measurement results. Finally, experimental difficulties are outlined and future directions are presented.

## 4.1 Device Description

### 4.1.1 Design Considerations

The nanowire QD consists of three parts: an InAsP QD, contained within an InP core, covered by InP cladding:

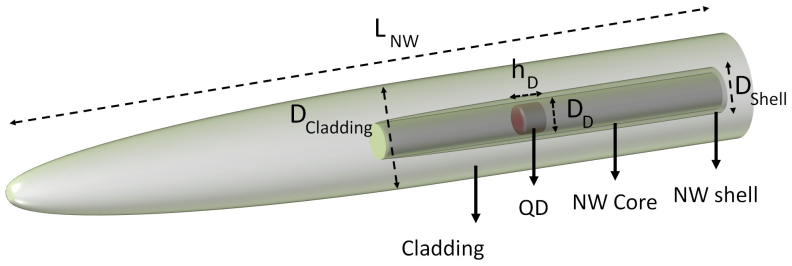


Figure 4.1: Nanowire QD schematic.

The core and cladding were designed to act as a cylindrical waveguide, supporting several guided modes around the QD emission wavelength of 950 nm. This waveguide structure allows for broadband emission, which is more forgiving to design imperfections than narrowband micro-cavities used previously [48]. A taper is included at the end of the nanowire waveguide, allowing for a gradual decrease in refractive index, minimizing reflection at the tip [47]. This novel design allows for collection efficiencies exceeding 90%.

In addition, careful monitoring of the electronic environment of the QD allows for unprecendented narrow emission linewidths (typically 30 $\mu$eV). This is achieved by minimizing charge fluctuations in the vicinity of the QD which generate a Stark shift in the emission

resonance. Such a shift is evidenced by spectral instability, and linewidth broadening referred to as spectral diffusion. The QD is protected from electric field fluctuations in two ways: first, the cladding eliminates surface states, such as dangling bonds, that would otherwise form on the QD surface. Secondly, stacking faults, which are interfaces between different crystalline structures in the nanowire material, are minimized along the nanowire axis. Stacking faults act as extremely efficient charge traps and should be minimized to obtain a clean emission [49].

### 4.1.2 Fabrication Overview

The nanowire QD sample was fabricated by our collaborator D. Dalacu at NRC, who has previous experience fabricating similar devices [50], [48]. The nanowires were created using a bottom-up fabrication approach and a novel vapour-liquid-solid (VLS) growth mechanism by our colleagues in the group of Ray LaPierre at McMaster University. First, the InP core containing the InAsP QD is grown, ensuring that each nanowire contains only one QD that is ideally located at the center of the nanowire axis. The inner core region then seeds the growth of the outer cladding and determines its overall crystal purity [51]. Historically, InP nanowires grown using a bottom-up approach are polytypic, meaning they contain alternating sections of zinc-blende (ZB) and wurtzite (WZ) crystal structures [52]. This new approach reduces the number of stacking faults to $< 1$ $/\mu m$, with zero stacking faults on average for a 750 nm tall nanowire [51]. This reduction in stacking faults helps to reduce the local charge fluctuation around the QD, reducing excitonic linewidths by an order of magnitude [51].

An SEM image of the fabricated nanowire QD sample can be seen in Figure 4.2:

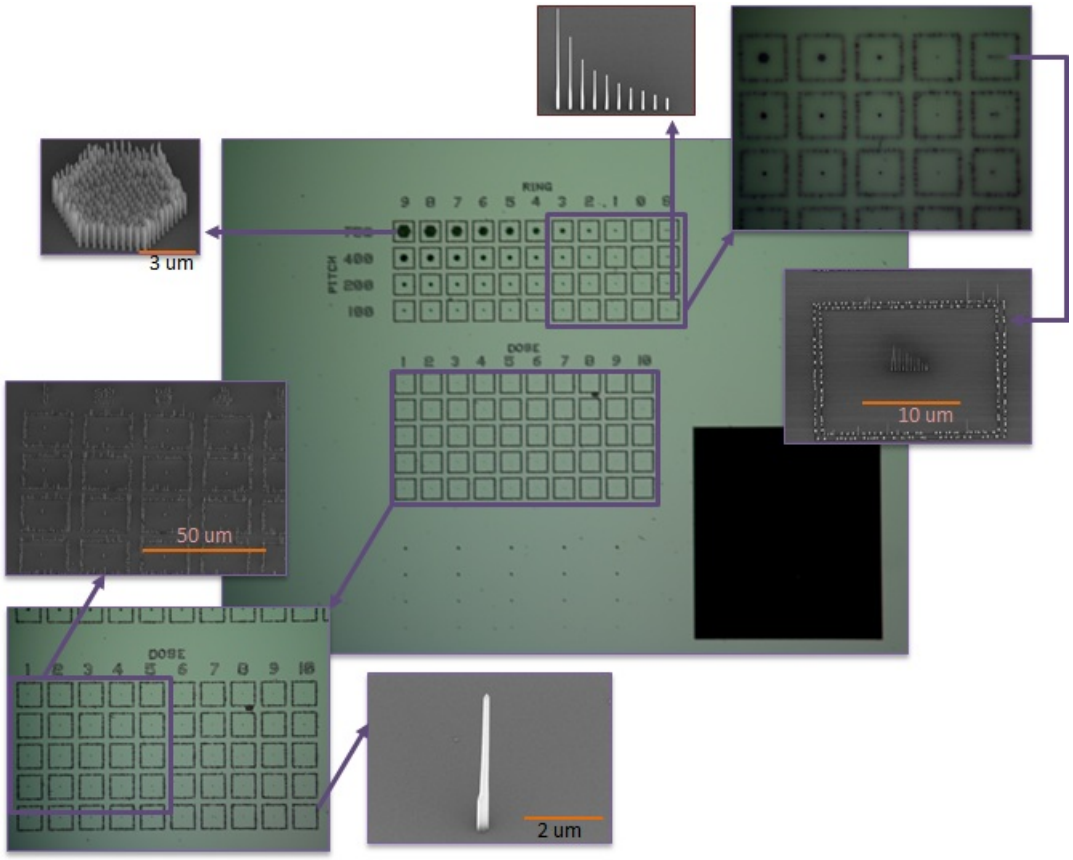


Figure 4.2: One region of the nanowire QD sample.

The sample consists of four regions, similar to the one shown in Figure 4.2, each corresponding to a different electron-beam lithography dose. In the top section, there is an array of 20 $\mu m$ X 20 $\mu m$ boxes, each containing a hexagonal group of nanowires which were used for experimental alignment and calibration. The central array of boxes each contain a single nanowire QD; the squares surrounding each individual nanowire are extremely bright when optically excited and assist in locating individual devices. The third region, which appears as a black square in Figure 4.2, is a dense region of nanowires (spacing of ~400 nm), which will be used in future work. The entire sample measures approximately 1 cm X 1 cm.

### 4.1.3 Initial Spectra

Several copies of the sample seen in Figure 4.2 were created by our colleagues at NRC, who performed some initial spectral measurements. A coarse PL measurement of a single nanowire QD at varying excitation powers can be seen in Figure 4.3 [51]:

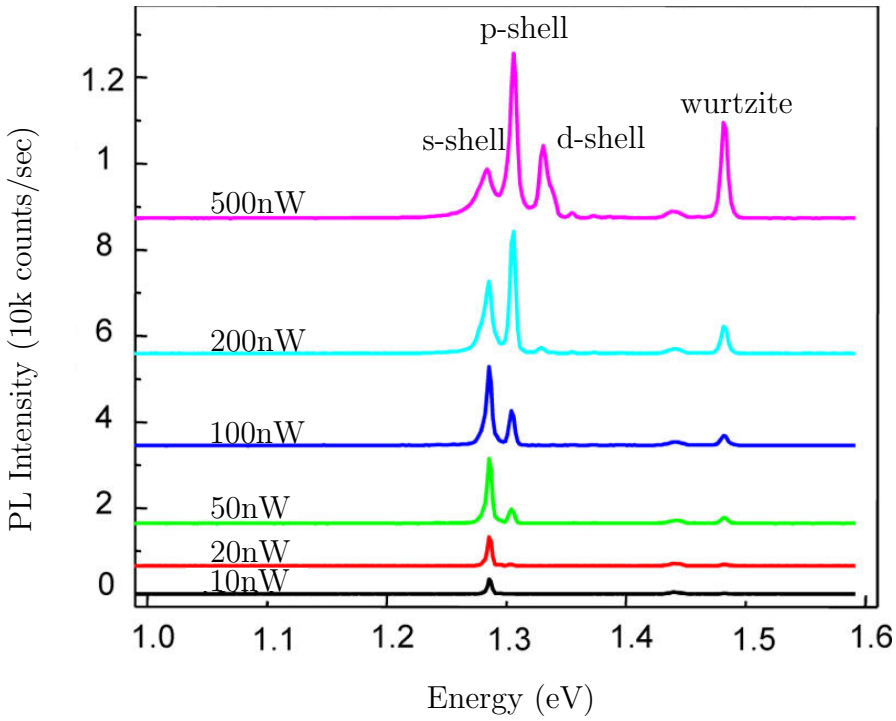


Figure 4.3: Coarse PL measurement of a single nanowire QD at varying excitation power.

The s-shell, p-shell, and d-shell resonances represent the ground state and first two excited state transitions of the QD, analogous to atomic orbitals. There is an additional peak at 1.49 eV (832 nm) for an empty nanowire, corresponding to the band-to-band electron-hole recombination in wurtzite InP. At low excitation power, an emission from the s-shell transition emerges as 1.30 eV (954 nm). As the power increases, the p-shell and d-shell transitions occur at 1.32 eV (939 nm) and 1.345 eV (922 nm) respectively. As higher

orbital transitions appear, the lower order transitions are quenched; a possible reason for this is the slower electron relaxation time relative to the hole relaxation, which causes the excitonic recombination path to be dictated by the highest occupied hole level [53]. When an electron relaxes to this level it will recombine, never reaching the low level orbitals. A high resolution image of the s-shell transition from a single QD can be seen in Figure 4.4:

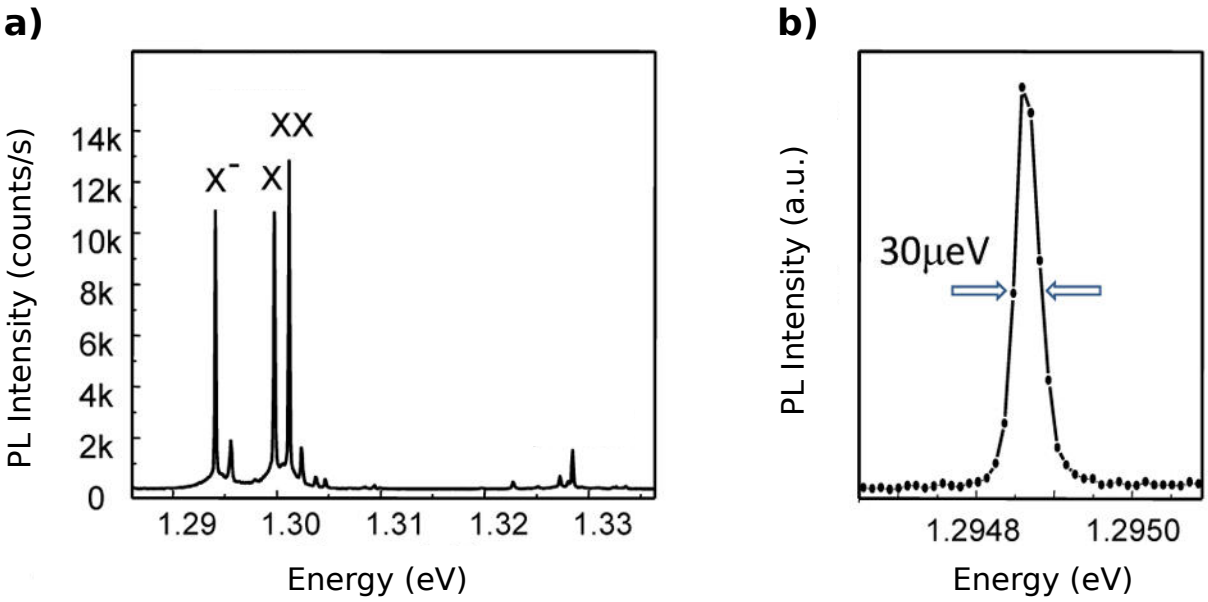


Figure 4.4: a) High resolution image of the s-shell transition from a single QD pumped at saturation b) Low excitation power spectrum of a charge exciton with narrow emission linewidth [51].

The three peaks in Figure 4.4 consist of the single exciton (X), biexciton (XX), and charged exciton ($X^-$) emission resonances [51]. The X and XX transitions are separated by $< 1$ nm, necessitating a high resolution spectrometer resolution to differentiate the two peaks.

## 4.2 Experimental Goals

There were four major experimental goals to achieve with the nanowire QD sample:

1. The first goal was to obtain a coarse resolution power dependent spectra of a single QD. The power should be varied to determine when the s-shell transitions are saturated and the p-shell transitions emerge. Excitation power for future measurements should be kept below this value to ensure operation in the single photon regime.

2. The second goal was to obtain a high resolution spectrum from a QD, using a pump power that is below the s-shell saturation value. All three excitonic transitions should be fully resolved.

3. The third goal was to measure the s-shell evolution with power. This would provide intuition as to how the excitonic population within the s-shell varies as a function of power.

4. The last goal involved gathering photon statistic for a single exciton emission using an HBT setup. This would verify that the QD is acting as a true single photon emitter.

## 4.3 Measurements

All measurements were conducted using a home-built confocal microscope, where the sample was mounted in a Janis ST-500 helium flow cryostat and cooled to 4 K. Excitation was achieved using a 532 nm CW laser. A similar setup is seen in Figure 2.7.

### 4.3.1 Nanowire Emission

The InP nanowire containing the QD has an emission signature that can be seen in Figure 4.5. This spectrum was collected using a 150 lines/mm spectrometer grating, with a 1 mm slit width.

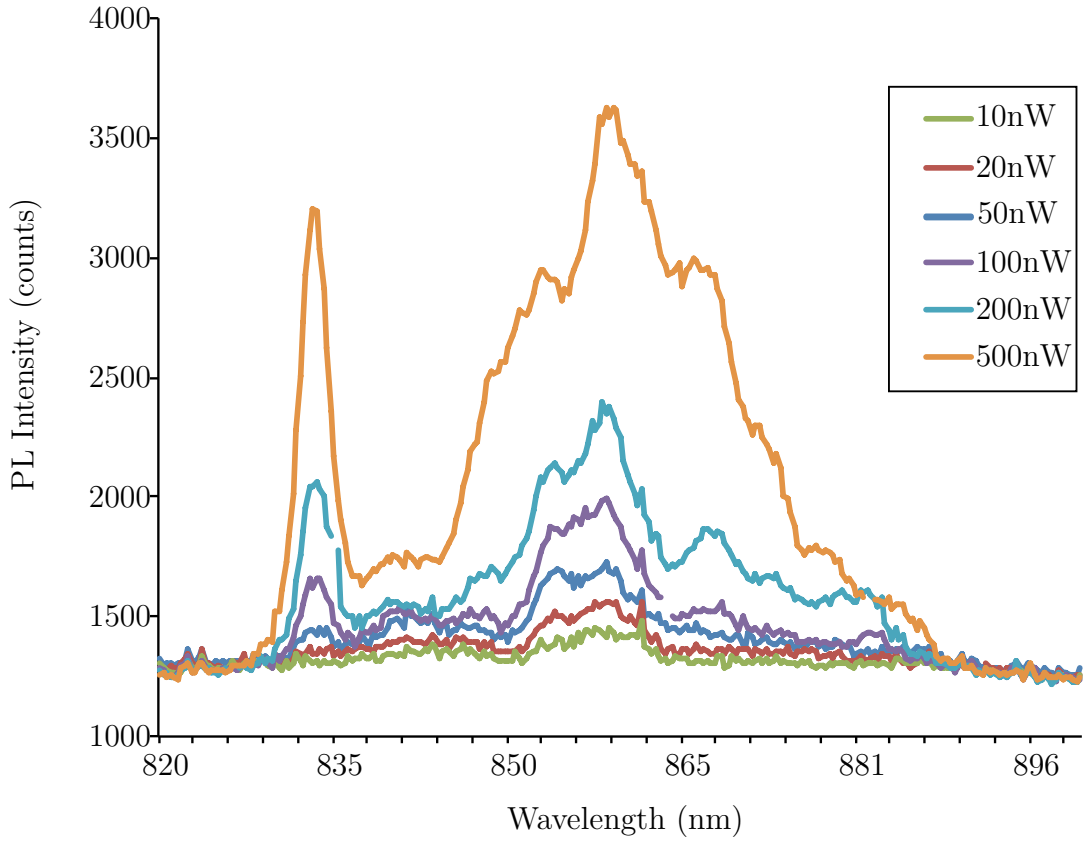


Figure 4.5: Nanowire and acceptor state emission spectrum at varying pump powers.

Due to the absence of stacking faults, one would expect minimal signs of polytypism (segmented sections of WZ and ZB crystal structure) in the nanowire emission [52]. Figure 4.5 exhibits a sharp emission at 832 nm, which is cited in literature as excitonic recombination of bulk-like InP [49]. With increasing optical pump power, there is an emergence of fluorescence centered at 860 nm that can be attributed to band-acceptor and donor-acceptor recombination in WZ InP. This type of recombination is often followed by optical phonon replication, and the weak emission at 886 nm corroborates this [49]. This nanowire emission appears at very low excitation power, and add unwanted background fluorescence. This emission can be filtered out using a 900-1375 nm band-pass filter to isolate the QD

emission.

### 4.3.2 Quantum Dot Emission

Spectra from the nanowire QD sample was acquired using a 1200 lines/mm spectrometer grating, which was measured to have reasonably high efficiency for both TE and TM polarized light at 950 nm. First, it was important to determine the QD spectral evolution with respect to pump power, noting the power required to saturate the s-shell transitions. The pump power should be kept below this value for single photon emission. Figure 4.6 shows the spectral evolution taken with a 0.5 mm spectrometer slit width:

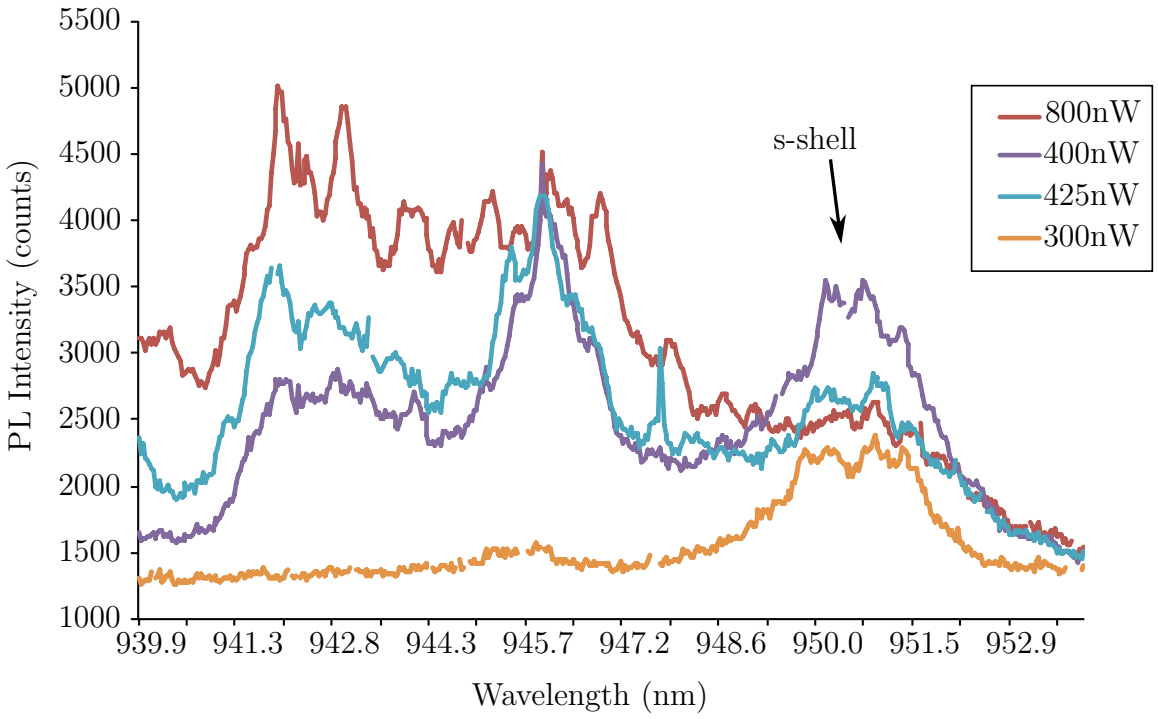


Figure 4.6: Spectral evolution of a nanowire QD at varying pump powers.

The resolution of this plot is too low to fully resolve the X and XX s-shell transitions, but took several minutes to acquire given the efficiency of the setup and spectrometer at 950 nm. The spectrometer resolution was tested using an Ar gas lamp, which has extremely narrow emission resonances at 912.297 nm and 922.45 nm. At these wavelengths, the resolution is certainly limited by the spectrometer, and was shown to be 0.7 nm under the conditions of Figure 4.6. The resolution is not high enough to fully resolve the X and XX excitonic transitions which are separated by roughly 1 nm. In an attempt to test the resolution, an experiment was performed where the pump power was kept constant at a value below the s-shell saturation limit, and the slit width was narrowed. The results can be seen in Figure 4.7:

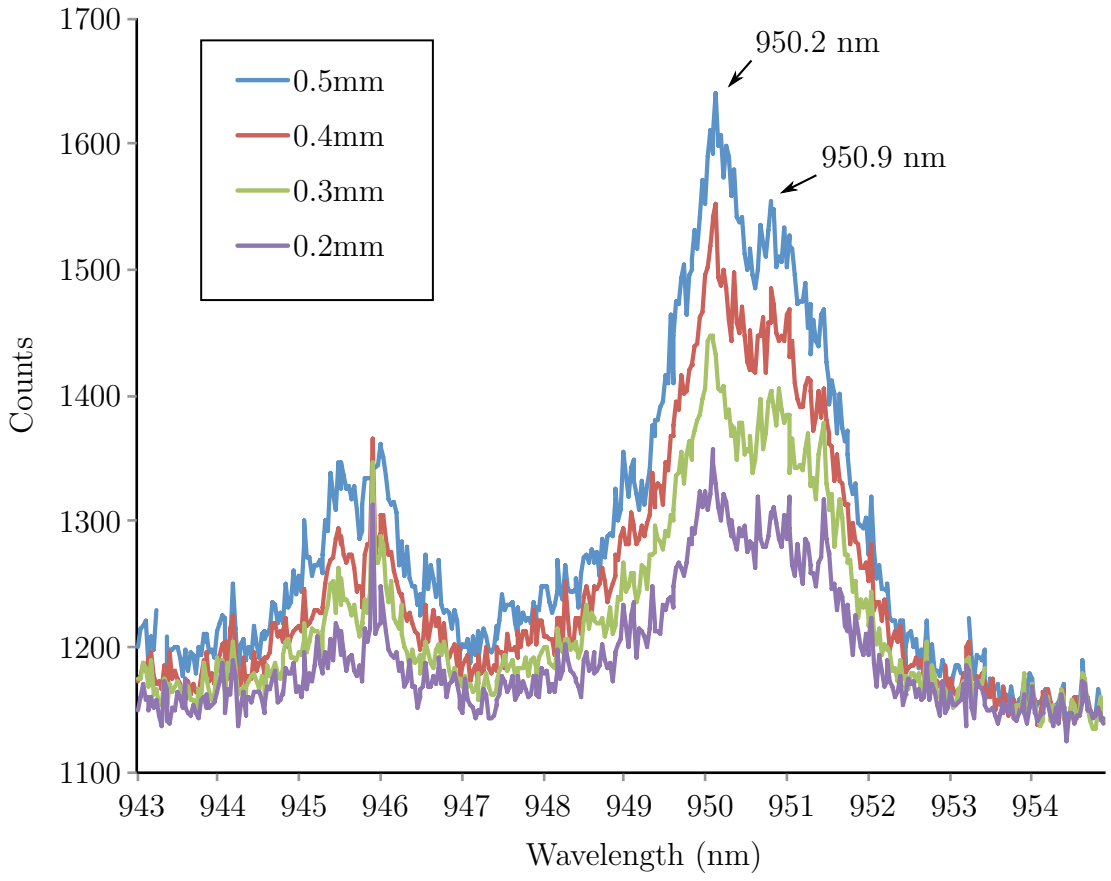


Figure 4.7: Exciton and biexciton s-shell transitions for a constant pump power and varied spectrometer slit width.

The expected linewidths of the X and XX transitions are very narrow (<100 $\mu eV$), as the nanowires are of high structural quality and free of stacking faults. If the resolution is limited by the spectrometer, decreasing the slit width should increase the resolution, and decrease the signal intensity. In Figure 4.7 it is clear that decreasing the slit width does not cause a dramatic increase in resolution for the measured excitonic transitions. This implies that the broadened excitonic linewidths are a true artifact of the QD emission, and are not caused by the low resolution spectrometer. We suggest that the broadening is due to the off-resonant pump laser. The QDs were excited using a 532 nm CW laser, which is far off of the 950 nm expected emission. This above-band excitation is expected to cause local charge fluctuations around the QD structure, causing spectral diffusion and broadening the excitonic linewidths. Higher collection efficiency and resonant excitation are necessary for narrow emission linewidths suitable for indistinguishable photon generation.

## 4.4 Experimental Challenges

Only the first experimental goal was completed, as evidenced by the measurements in Section 4.3.2. There were several experimental challenges faced in achieving even this coarse spectrum. First, the measurements were taken using a confocal microscope system originally designed for observation of nitrogen vacancy centers. Such a system is created for optical pumping at 532 nm and collection at 637 nm, which is quite far off the expected QD emission of 950 nm. Only the minimum number of components were changed in the setup to maintain its general alignment for other applications. The microscope included a 800 nm short-pass filter, 650 nm long pass filter, and 532 nm notch filter to remove residual laser light. The 800 nm and 532 nm filters were both removed to allow for transmission of the 950 nm QD emission, and were replaced with a 900-1375 nm band-pass filter to isolate the excitonic emission from the residual laser light. This filter had 90% transmission at 950 nm and blocked 87% at 532 nm.

In addition to switching out filters with poor spectral response, the single mode fiber (SMF) in the collection arm of the microscope was changed to multi-mode fiber (MMF). The original SMF, which was purchased for collection at 637 nm, was unable to support

optical modes at 950 nm. Consequently, a MMF was chosen that could support modes over a broad range of wavelengths. With this change, we were finally able to observe resonant peaks around 950 nm with a spectrometer, but acquisition took several minutes with the lowest resolution grating.

Another source of inefficiency was the spectrometer used to analyze the QD emission. We used the Horiba iHr 550 spectrometer, equipped with a synapse open-electrode CCD detector. The efficiency of the CCD detector is 48% at 830 nm and drops to 20% at 950 nm, making it very inefficient for collecting QD emission in the near-IR range. The spectrometer is equipped with three different gratings (150 lines/mm, 1200 lines/mm, and 1800 lines/mm), to obtain different resolutions at the expense of decreased signal. The gratings are intended for use in the visible range with efficiencies quoted up to 800 nm; the efficiency is expected to decrease at higher wavelengths. High resolution spectra are acquired through optimization of both the spectrometer slit width and fine spectral gratings; for the highest resolution a small slit width and a high resolution grating are required, at the cost of signal power.

Finally, there were major issues with stage stability. Our measurements were conducted at liquid helium temperatures, in the Janis ST-500 helium flow cryostat. The flow was achieved by connecting a transfer line between the cryostat and a dewer of helium. Any vibrations in either the transfer line or dewer would shift the stage slightly, and the beam spot would move off the device of interest. Even a sub-micron movement is problematic for our measurements, which would sometimes take over thirty minutes to integrate.

## 4.5 Conclusion and Future Directions

The setup used to take the preliminary QD measurements lacks the efficiency and resolution required to do the experiments of interest involving single photons from the s-shell transitions. Several changes must be made to facilitate such experiments:

1. A setup should include optical components that are optimized for near-IR confocal

microscopy. Although we were able to get a signal using a setup intended for visible wavelengths, the inefficiencies of all the components contribute to the small number of photons collected.

2. A near-resonant laser should be used to excite the QDs. If the discrepancy in pump and emission wavelengths is too high, spectral diffusion broadens the emission line width.

3. A spectrometer with gratings and a detector that are suitable for 950 nm emission should be employed.

The project is ongoing and has since moved to Dr. Gregor Weihs' Lab at the Institute for Experimental Physics at the University of Innsbruck. This lab has the appropriate equipment for experiments involving quantum dots in the near-IR.

# Chapter 5

# Conclusion

This report discussed low temperature spectroscopy for two different solid state quantum systems: the nitrogen vacancy (NV) center in diamond and the semiconductor nanowire quantum dot.

First, the implementation of a resonant excitation spectroscopy setup for NV centers was outined, and some prelimary measurements were provided. Additionally, some promising results for an anti-reflection coating created for diamond were presented. This coating was shown to overcome total internal reflection at the air-diamond interface, increasing the number of photons collected from an NV center. Finally, some spectroscopic measurements for a novel InAsP nanowire quantum dot design were discussed.

Control and coupling of individual quantum systems in the solid state remains an important research area in experimental quantum information. Much of the work discussed in this thesis is on-going, but offers potential for long-range interaction between individual quantum systems in the solid state. It is important to continue engineering optical control techniques for such systems to achieve a regime suitable for applications in quantum information, such as long-distance entanglement.

# Appendix A

# Background Photoluminescence Calculation

To calculate the background contribution to the photon counts measured from an NV center at a specific pump power, one must extract data from the photon second order correlation function ($g^{(2)}(\tau)$), measured using a Hanbury Brown and Twiss (HBT) setup. The HBT setup is used to measured time delay between emitted photons, revealing the photon statistics of the source. The procedure can be illustrated with an example calculation for plasmonic aperture device excited with P=0.33 mW. The second order correlation data can be seen in Figure A.1:

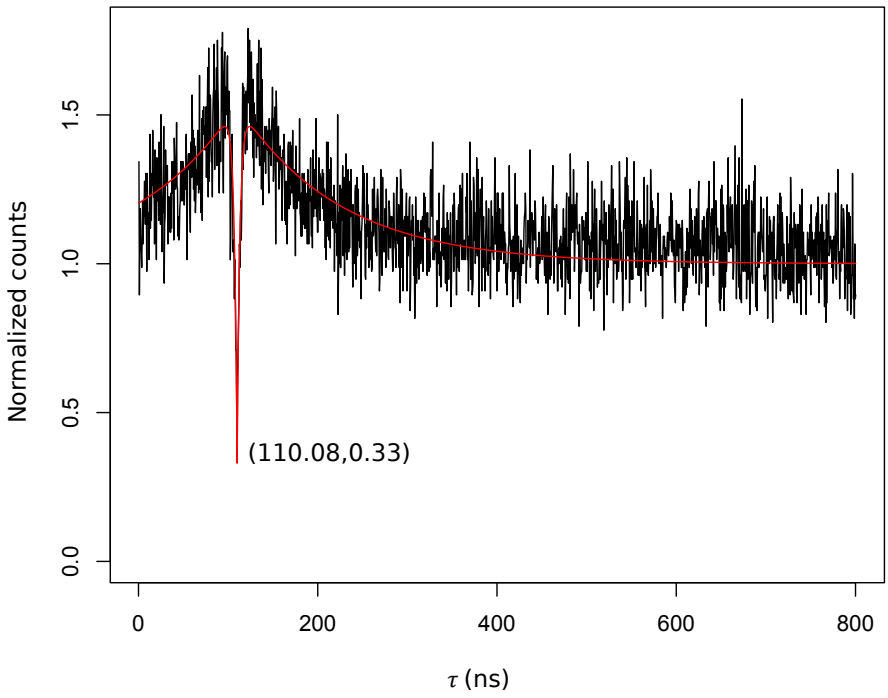


Figure A.1: $g^{(2)}(\tau)$ data for the silver aperture sample excited with P= 0.33 mW

The $g^{(2)}(\tau)$ data can be fit to the following equation [2]:

$$g^{(2)}(\tau) = A\Big[1 + C_2 \times exp(-\frac{|\tau - t_0|}{\tau_2}) + C_3 \times exp(-\frac{|\tau - t_0|}{\tau_3})\Big] \tag{A.1}$$

Where $A$, $C_2$, $C_3$, $\tau_2$, and $\tau_3$ are constant fitting parameters. The dip from the normalized second order correlation curve ($g^{(2)}(\tau)/A$) can be used to determine the signal to background ratio for the raw photon counts. This is achieved by calculating the corrected $g^{(2)}(\tau)$ function, $g_c^{(2)}(\tau)$, where background contributions have been eliminated. The correction is calculated using the following equation [3], [54]:

$$g_c^{(2)}(\tau) = \frac{[C_N(\tau) - (1 - \rho^2)]}{\rho^2} \tag{A.2}$$

Where $C_N(\tau)$ is the normalized count rate and $\rho = \frac{S}{S+B}$ is the signal to background ratio.

For an ideal single-photon source, $g_c^{(2)}(0) = 0$, and Equation A.2 becomes:

$$\begin{aligned} C_N(0) &= 1 - \rho^2 \\ \rho &= \sqrt{1 - C_N(0)} \\ \frac{S}{S+B} &= \sqrt{1 - C_N(0)} \\ \frac{B}{S+B} &= 1 - \sqrt{1 - C_N(0)} \end{aligned} \tag{A.3}$$

The background can be estimated using the raw photon count value and Equation A.3. For the device excited with a 0.33 mW pump laser, $C_N(0) = 0.33$:

$$\begin{aligned} \frac{B}{S+B} &= 1 - \sqrt{1 - C_N(0)} \\ &= 0.181 \end{aligned}$$

The total background contribution can be calculated by multiplying this ratio with the total raw photon counts collected at that pump power. The background can then be linearly interpolated from the set of calculated background counts. Finally, the net photon counts can be calculated by subtracting the background contribution from the raw data.

# Bibliography


[1] B. Hausmann, *Nanophotonics in Diamond*. PhD thesis, Harvard University, May 2013.

[2] C. Kurtsiefer, S. Mayer, P. Zarda, and H. Weinfurter, "Stable solid-state source of single photons," *Phys. Rev. Lett.*, vol. 85, pp. 290–293, 07/10 2000.

[3] A. Beveratos, R. Brouri, T. Gacoin, J.-P. Poizat, and P. Grangier, "Nonclassical radiation from diamond nanocrystals," *Phys. Rev. A*, vol. 64, p. 061802, 11/19 2001.

[4] G. Balasubramanian, P. Neumann, D. Twitchen, M. Markham, R. Kolesov, N. Mizuochi, J. Isoya, J. Achard, J. Beck, J. Tissler, V. Jacques, P. R. Hemmer, F. Jelezko, and J. Wrachtrup, "Ultralong spin coherence time in isotopically engineered diamond.," *Nature Mater.*, vol. 8, pp. 383–7, May 2009.

[5] P. Neumann, J. Beck, M. Steiner, F. Rempp, H. Fedder, P. R. Hemmer, J. Wrachtrup, and F. Jelezko, "Single-shot readout of a single nuclear spin.," *Science*, vol. 329, pp. 542–4, July 2010.

[6] V. Jacques, P. Neumann, J. Beck, M. Markham, D. Twitchen, J. Meijer, F. Kaiser, G. Balasubramanian, F. Jelezko, and J. Wrachtrup, "Dynamic Polarization of Single Nuclear Spins by Optical Pumping of Nitrogen-Vacancy Color Centers in Diamond at Room Temperature," *Phys. Rev. Lett.*, vol. 102, p. 057403, Feb. 2009.

[7] B. Smeltzer, J. McIntyre, and L. Childress, "Robust control of individual nuclear spins in diamond," *Phys. Rev. A*, vol. 80, p. 050302, Nov. 2009.

[8] P. C. Maurer, G. Kucsko, C. Latta, L. Jiang, N. Y. Yao, S. D. Bennett, F. Pastawski, D. Hunger, N. Chisholm, M. Markham, D. J. Twitchen, J. I. Cirac, and M. D. Lukin, "Room-temperature quantum bit memory exceeding one second.," *Science*, vol. 336, pp. 1283–6, June 2012.

[9] H. Bernien, B. Hensen, W. Pfaff, G. Koolstra, M. S. Blok, L. Robledo, T. H. Taminiau, M. Markham, D. J. Twitchen, L. Childress, and R. Hanson, "Heralded entanglement between solid-state qubits separated by three metres.," *Nature*, vol. 497, pp. 86–90, May 2013.

[10] E. Togan, Y. Chu, A. S. Trifonov, L. Jiang, J. Maze, L. Childress, M. V. G. Dutt, A. S. Sø rensen, P. R. Hemmer, A. S. Zibrov, and M. D. Lukin, "Quantum entanglement between an optical photon and a solid-state spin qubit.," *Nature*, vol. 466, pp. 730–4, Aug. 2010.

[11] A. Sipahigil, M. L. Goldman, E. Togan, Y. Chu, M. Markham, D. J. Twitchen, A. S. Zibrov, A. Kubanek, and M. D. Lukin, "Quantum Interference of Single Photons from Remote Nitrogen-Vacancy Centers in Diamond," *Phys. Rev. Lett.*, vol. 108, p. 143601, Apr. 2012.

[12] H. Bernien, L. Childress, L. Robledo, M. Markham, D. Twitchen, and R. Hanson, "Two-Photon Quantum Interference from Separate Nitrogen Vacancy Centers in Diamond," *Phys. Rev. Lett.*, vol. 108, p. 043604, Jan. 2012.

[13] C. K. Hong, Z. Y. Ou, and L. Mandel, "Measurement of subpicosecond time intervals between two photons by interference," *Phys. Rev. Lett.*, vol. 59, pp. 2044–2046, Nov. 1987.

[14] A. Lenef and S. Rand, "Electronic structure of the N-V center in diamond: Theory," *Phys. Rev. B*, vol. 53, pp. 13441–13455, May 1996.

[15] N. B. Manson, J. P. Harrison, and M. J. Sellars, "Nitrogen-vacancy center in diamond: Model of the electronic structure and associated dynamics," *Phys. Rev. B*, vol. 74, p. 104303, Sep 2006.

[16] A. Batalov, V. Jacques, F. Kaiser, P. Siyushev, P. Neumann, L. J. Rogers, R. L. McMurtrie, N. B. Manson, F. Jelezko, and J. Wrachtrup, "Low temperature studies of the excited-state structure of negatively charged nitrogen-vacancy color centers in diamond," *Phys. Rev. Lett.*, vol. 102, p. 195506, May 2009.

[17] M. W. Doherty, N. B. Manson, P. Delaney, and L. C. L. Hollenberg, "The negatively charged nitrogen-vacancy centre in diamond: the electronic solution," *New J. Phys.*, vol. 13, p. 025019, Feb. 2011.

[18] P. Tamarat, N. B. Manson, J. P. Harrison, R. L. McMurtrie, A. Nizovtsev, C. Santori, R. G. Beausoleil, P. Neumann, T. Gaebel, F. Jelezko, P. Hemmer, and J. Wrachtrup, "Spin-flip and spin-conserving optical transitions of the nitrogen-vacancy centre in diamond," *New J. Phys.*, vol. 10, 2008.

[19] L. J. Rogers, S. Armstrong, M. J. Sellars, and N. B. Manson, "Infrared emission of the NV centre in diamond: Zeeman and uniaxial stress studies," *New J. Phys.*, vol. 10, p. 103024, Oct. 2008.

[20] F. Jelezko, I. Popa, A. Gruber, C. Tietz, J. Wrachtrup, A. Nizovtsev, and S. Kilin, "Single spin states in a defect center resolved by optical spectroscopy," *Appl. Phys. Lett.*, vol. 81, no. 12, pp. 2160–2162, 2002.

[21] K.-M. C. Fu, C. Santori, P. E. Barclay, and R. G. Beausoleil, "Conversion of neutral nitrogen-vacancy centers to negatively charged nitrogen-vacancy centers through selective oxidation," *Appl. Phys. Lett.*, vol. 96, p. 121907, Mar. 2010.

[22] C. Santori, P. Barclay, K.-M. Fu, and R. Beausoleil, "Vertical distribution of nitrogen-vacancy centers in diamond formed by ion implantation and annealing," *Phys. Rev. B*, vol. 79, p. 125313, Mar. 2009.

[23] A. Stacey, T. J. Karle, L. P. McGuinness, B. C. Gibson, K. Ganesan, S. Tomljenovic-Hanic, A. D. Greentree, A. Hoffman, R. G. Beausoleil, and S. Prawer, "Depletion of nitrogen-vacancy color centers in diamond via hydrogen passivation," *Appl. Phys. Lett.*, vol. 100, p. 071902, Feb. 2012.

[24] S. Cui and E. L. Hu, "Effect of fluorinated diamond surface on charge state of nitrogen-vacancy centers," Apr. 2013.

[25] P. Siyushev, H. Pinto, M. Vörös, A. Gali, F. Jelezko, and J. Wrachtrup, "Optically Controlled Switching of the Charge State of a Single Nitrogen-Vacancy Center in Diamond at Cryogenic Temperatures," *Phys. Rev. Lett.*, vol. 110, p. 167402, Apr. 2013.

[26] N. Manson and J. Harrison, "Photo-ionization of the nitrogen-vacancy center in diamond," *Diamond Relat. Mater.*, vol. 14, pp. 1705–1710, Oct. 2005.

[27] T. Gaebel, M. Domhan, C. Wittmann, I. Popa, F. Jelezko, J. Rabeau, A. Greentree, S. Prawer, E. Trajkov, P. Hemmer, and J. Wrachtrup, "Photochromism in single nitrogen-vacancy defect in diamond," *Appl. Phys. B*, vol. 82, pp. 243–246, Nov. 2005.

[28] T. M. Babinec, B. J. M. Hausmann, M. Khan, Y. Zhang, J. R. Maze, P. R. Hemmer, and M. Loncar, "A diamond nanowire single-photon source.," *Nature Nano.*, vol. 5, pp. 195–9, Mar. 2010.

[29] B. J. Hausmann, M. Khan, Y. Zhang, T. M. Babinec, K. Martinick, M. McCutcheon, P. R. Hemmer, and M. Lončar, "Fabrication of diamond nanowires for quantum information processing applications," *Diamond Relat. Mater.*, vol. 19, pp. 621–629, May 2010.

[30] J. T. Choy, B. J. M. Hausmann, T. M. Babinec, I. Bulu, M. Khan, P. Maletinsky, A. Yacoby, and M. Loncar, "Enhanced single-photon emission from a diamond-silver aperture," *Nature Photon.*, vol. 5, pp. 738–743, print 2011.

[31] J. Choy, I. Bulu, B. Hausmann, E. Janitz, I. Huang, and M. Loncar, "Spontaneous emission and collection efficiency enhancement of single photon emitters in diamond via plasmonic cavity and grating," *Submitted to App. Phys. Lett.*, 2013.

[32] L. Robledo, L. Childress, H. Bernien, B. Hensen, P. F. A. Alkemade, and R. Hanson, "High-fidelity projective read-out of a solid-state spin quantum register.," *Nature*, vol. 477, pp. 574–8, Sept. 2011.

[33] N. Manson and J. Harrison, "Photo-ionization of the nitrogen-vacancy center in diamond," *Diamond Relat. Mater.*, vol. 14, pp. 1705–1710, Oct. 2005.

[34] L. Robledo, H. Bernien, I. van Weperen, and R. Hanson, "Control and Coherence of the Optical Transition of Single Nitrogen Vacancy Centers in Diamond," *Phys. Rev. Lett.*, vol. 105, p. 177403, Oct. 2010.

[35] F. Kaiser, V. Jacques, A. Batalov, P. Siyushev, F. Jelezko, and J. Wrachtrup, "Polarization properties of single photons emitted by nitrogen-vacancy defect in diamond at low temperature," p. 4, June 2009.

[36] K.-M. C. Fu, C. Santori, P. E. Barclay, L. J. Rogers, N. B. Manson, and R. G. Beausoleil, "Observation of the Dynamic Jahn-Teller Effect in the Excited States of Nitrogen-Vacancy Centers in Diamond," *Phys. Rev. Lett.*, vol. 103, p. 256404, Dec. 2009.

[37] P. Siyushev, F. Kaiser, V. Jacques, I. Gerhardt, S. Bischof, H. Fedder, J. Dodson, M. Markham, D. Twitchen, F. Jelezko, and J. Wrachtrup, "Monolithic diamond optics for single photon detection," *Appl. Phys. Lett.*, vol. 97, no. 24, p. 241902, 2010.

[38] CVI Melles Griot, *Technical Guide*, 2nd ed., 2009.

[39] A. F. Oskooi, D. Roundy, M. Ibanescu, P. Bermel, J. Joannopoulos, and S. G. Johnson, "Meep: A flexible free-software package for electromagnetic simulations by the fdtd method," *Comput. Phys. Commun.*, vol. 181, no. 3, pp. 687 – 702, 2010.

[40] R. J. Epstein, F. M. Mendoza, Y. K. Kato, and D. D. Awschalom, "Anisotropic interactions of a single spin and dark-spin spectroscopy in diamond," *Nature Phys.*, vol. 1, pp. 94–98, print 2005.

[41] W. Lukosz, "Light emission by magnetic and electric dipoles close to a plane dielectric interface. III. radiation patterns of dipoles with arbitrary orientation," *J. Opt. Soc. Am.*, vol. 69, pp. 1495–1503, Nov 1979.

[42] D. Le Sage, L. M. Pham, N. Bar-Gill, C. Belthangady, M. D. Lukin, A. Yacoby, and R. L. Walsworth, "Efficient photon detection from color centers in a diamond optical waveguide," *Phys. Rev. B*, vol. 85, p. 121202, Mar 2012.

[43] E. Knill, R. Laflamme, and G. J. Milburn, "A scheme for efficient quantum computation with linear optics.," *Nature*, vol. 409, pp. 46–52, Jan. 2001.

[44] P. Michler, A. Kiraz, C. Becher, W. V. Schoenfeld, P. M. Petroff, L. Zhang, E. Hu, and A. Imamoglu, "A quantum dot single-photon turnstile device.," *Science (New York, N.Y.)*, vol. 290, pp. 2282–5, Dec. 2000.

[45] R. Bratschitsch and A. Leitenstorfer, "Quantum dots: artificial atoms for quantum optics.," *Nature Mater.*, vol. 5, pp. 855–6, Nov. 2006.

[46] P. Michler, *Single Quantum Dots: Fundamentals, Applications and New Concepts.* Germany: Springer, 2003.

[47] J. Claudon, J. Bleuse, N. S. Malik, M. Bazin, P. Jaffrennou, N. Gregersen, C. Sauvan, P. Lalanne, and J.-M. Gérard, "A highly efficient single-photon source based on a quantum dot in a photonic nanowire," *Nature Photon.*, vol. 4, pp. 174–177, Jan. 2010.

[48] M. E. Reimer, G. Bulgarini, N. Akopian, M. Hocevar, M. B. Bavinck, M. A. Verheijen, E. P. A. M. Bakkers, L. P. Kouwenhoven, and V. Zwiller, "Bright single-photon sources in bottom-up tailored nanowires.," *Nat. Commun.*, vol. 3, p. 737, Jan. 2012.

[49] E. G. Gadret, G. O. Dias, L. C. O. Dacal, M. M. de Lima, C. V. R. S. Ruffo, F. Iikawa, M. J. S. P. Brasil, T. Chiaramonte, M. A. Cotta, L. H. G. Tizei, D. Ugarte, and A. Cantarero, "Valence-band splitting energies in wurtzite InP nanowires: Photoluminescence spectroscopy and *ab initio* calculations," *Phys. Rev. B*, vol. 82, p. 125327, Sep 2010.

[50] D. Dalacu, K. Mnaymneh, X. Wu, J. Lapointe, G. C. Aers, P. J. Poole, and R. L. Williams, "Selective-area vapor-liquid-solid growth of tunable InAsP quantum dots in nanowires," *Appl. Phys. Lett.*, vol. 98, no. 25, p. 251101, 2011.

[51] D. Dalacu, K. Mnaymneh, J. Lapointe, X. Wu, P. J. Poole, G. Bulgarini, V. Zwiller, and M. E. Reimer, "Ultraclean emission from InAsP quantum dots in defect-free wurtzite InP nanowires," *Nano Lett.*, vol. 12, no. 11, pp. 5919–5923, 2012.

[52] J. M. Jancu, K. Gauthron, L. Largeau, G. Patriarche, J. C. Harmand, and P. Voisin, "Type II heterostructures formed by zinc-blende inclusions in InP and GaAs wurtzite nanowires," *Appl. Phys. Lett.*, vol. 97, no. 4, p. 041910, 2010.

[53] N. Sköld, M.-E. Pistol, K. A. Dick, C. Pryor, J. B. Wagner, L. S. Karlsson, and L. Samuelson, "Microphotoluminescence studies of tunable wurtzite InAs0.85P0.15 quantum dots embedded in wurtzite InP nanowires," *Phys. Rev. B*, vol. 80, p. 041312, Jul 2009.

[54] R. Brouri, A. Beveratos, J.-P. Poizat, and P. Grangier, "Photon antibunching in the fluorescence of individual color centers in diamond," *Opt. Lett.*, vol. 25, pp. 1294–1296, 09/01 2000.